



universität
wien

DIPLOMARBEIT

Titel der Diplomarbeit

Polarization-modulated Fourier transform infrared spectroscopy of a polylactic acid film

verfasst von
Jakob Kilgus

angestrebter akademischer Grad
Magister der Naturwissenschaften (Mag.rer.nat.)

Linz, am 24. Jänner 2013

Studienkennzahl lt. Studienblatt: A 411

Studienrichtung lt. Studienblatt: Diplomstudium Physik

Betreut von: A.o. Univ.-Prof. Dr. Martin Fally

Danksagung

Im Laufe meines Studiums und meiner Diplomarbeit haben mir viele Menschen geholfen, welchen ich danken möchte. Vor allem aber bin ich dankbar dafür, dass es mir überhaupt möglich war zu studieren. Dieser Dank gebührt in erster Linie meiner Mutter, die mir fortwährend Unterstützung bot und nicht zuletzt mit ihren Englischkenntnissen eine große Hilfe beim Korrigieren dieser Arbeit war. Während meines Studiums bin ich zweifacher Vater geworden, und hätte mir meine Freundin Nora nicht oft Zeit zum Studieren zur Verfügung gestellt, wären Kinderbetreuung und Studium kaum erfolgreich verlaufen. Ein großer Dank gilt also meiner Familie Nora, Juri und Mattis, die mir unentwegt Kraft und Mut geben.

Ich machte meine Diplomarbeit bei der Firma RECENDT, wo mir kein einziger Stein in den Weg gelegt wurde. Ich erhielt fortlaufend Hilfe und vor allem die Möglichkeit wissenschaftlich experimentell zu arbeiten, wobei ich sehr viel lernen konnte. Ich möchte mich bei allen Kolleginnen und Kollegen für ihre große Unterstützung und die angenehme Arbeitsatmosphäre bedanken.

Meinem Betreuer Martin Fally gebührt ebenfalls großer Dank, nicht nur weil die Zusammenarbeit mit ihm so angenehm verlief, sondern vor allem weil er mit mir immer Geduld bewies und er immer zur Stelle war, wenn ich Rat benötigte.

Abstract

Fourier transform infrared (FTIR) spectroscopy is an established measurement technique in industrial process analysis, in which presently the measurement of the change of the polarization of the light, caused by the specimen (through reflection or transmission), is still largely neglected. Depending on the specific measurement setup used, the change of polarization, however, contains additional information about the probe, and polarization-dependent measurements generally lead to an increase in sensitivity.

In this work three different polarization-dependent measurement methods are applied in transmission, namely static as well as polarization-modulated infrared linear dichroism measurements (PM-IRLD), polarization-modulated spectroscopic ellipsometry (PMSE) and FTIR spectroscopy in crossed-polarizers configuration, in order to achieve information about the orientation of the molecules of a polylactic acid (PLA) film during a stretching process. The application of the polarization modulation promises an improvement in the measurement precision by compensation of environmental perturbations. In the course of this work a new, flexible, computer-controlled measurement setup with an appropriate digital signal processing unit and with connection to the existing FTIR spectrometer was built up. This setup enables the application of the various polarization-dependent measurement methods and is aimed at their advancement and implementation in the field of the industrial process.

The results clearly show that by means of the applied measurement methods the change of orientation of individual molecules of the PLA film during the stretching process can be observed. So far the various measurement methods highly differ in their signal-to-noise ratios, however, and concerning this matter the methods which apply polarization modulation need special improvements. Nonetheless the results show promise for further measurements related to process control and for the coming polarization-dependent reflection measurements, which can also be executed with the designed setup.

Contents

1. Introduction	1
2. Background	3
2.1 Material Properties	3
2.2 FTIR Spectroscopy	6
2.2.1 IR Spectroscopy	6
2.2.2 Principles of FTIR	8
2.2.3 FTIR Data Processing	12
2.3 Polarization of Light	14
2.3.1 Birefringence and Dichroism	14
2.3.2 Polarization Modulation	17
3. Methods and Materials	21
3.1 Methods	21
3.1.1 Phase-modulated IRLD	21
3.1.2 Phase-modulated Spectroscopic Ellipsometry	23
3.1.3 Calibration Procedure	26
3.2 Experimental Data Processing	28
3.3 Instrumentation	31
4. Results	35
4.1 The Stretching Device	35
4.2 IRLD	36
4.2.1 Static IRLD	36
4.2.2 Phase-modulated IRLD	41
4.3 Phase-modulated Spectroscopic Ellipsometry	43
4.4 Configuration Between Crossed Polarizers	45
4.5 Error Estimation	47
5. Conclusions	53
 A Jones Calculus	 55
B Mertz Method	57

1. Introduction

This thesis is part of a project funded by the BRIDGE-program of the Austrian Research Promotion Agency FFG¹, which is aimed at promoting projects at the interface of fundamental research and experimental development in industry. The research cooperation of science and economy shall succeed in advancement and economic utilization of scientific findings and as a consequence in an increase of innovation. The title of the project is ‘Polarization-dependent vibrational spectroscopy in industrial process control’². The partners in this project are on the one hand RECENDT³, an internationally renowned, non-university research center, accounted for the theoretical and experimental research in this project, and on the other hand i-RED Infrarotsysteme GmbH, a device manufacturer generating process control solutions based on their Fourier transform near-infrared process spectrometer. With the help of the industry partner the developed methods can be tested for their practicability for process implementation.

The aim of the project is the utilization of the advantages of polarization-dependent infrared (IR) spectroscopy for process control. These advantages over classical IR spectroscopy are on the one hand their high sensitivity and on the other hand the gain of additional information depending on the method used. By means of spectroscopic ellipsometry, for example, the complex refractive index and the thickness of layers can be determined, or as another example, by means of infrared linear dichroism (IRLD) measurements the orientation of individual molecules can be observed. Solely the state of polarization of the light and its change through transmission or reflection bring the additional structural information. Fourier transform infrared (FTIR) spectroscopy is a very powerful and popular technique to determine the conformation of materials. Its relatively low cost accompanies one of its greatest strengths, namely that samples in all phases of matter can be studied. FTIR spectroscopy with polarized light provides information about the orientation and the conformation of multicomponent systems simultaneously and makes FTIR spectroscopy an even more powerful technique.

At first a concise measurement setup in the laboratory at RECENDT has to be created, which can then be adapted with optical components suitable for industrial process control. This task is performed by means of this work building the starting point of the project. The laboratory setup with connection to the existing FTIR spectrometer will serve as reference method and will determine the difference in accuracy between the field of the laboratory and of the process. In this thesis

¹Österreichische Forschungsförderungsgesellschaft, <http://www.ffg.at/bridge>

²In German: ‘Polarisationsabhängige Schwingungsspektroskopie in der industriellen Prozessüberwachung’(PSiP)

³Research Center for Non Destructive Testing, <http://www.recendt.at/>

various optical transmission setups according to various methods are analyzed. In order to achieve highly accurate results a photoelastic modulator is implemented in these setups modulating the polarization of the infrared light. The main focus of this thesis has been put on the additional gain of information induced by the application of polarized light in FTIR spectroscopy.

2. Background

2.1 Material Properties

As specimen a polylactic acid (PLA) film was chosen, because primarily being a polymer it has valuable optical properties and secondly being a biodegradable plastic it has ecologically beneficial properties, which should be supported.

A polymer is a macromolecule consisting of many small repetitious molecules known as monomers linked together by covalent bonds. They form chains which may be linear or branched, and combine into three-dimensional networks leading to versatile structures. It is important to notice that the structure determines also the macroscopic properties. As different monomers contain different functional groups which actually perform a function that is reflected in all properties, the characterization of a polymer requires several parameters which need to be specified. Because of the extraordinary range of properties of polymeric materials a variety of analyzing techniques is used. As each functional group of a polymer possesses specific absorption bands in the infrared region of the spectrum, infrared spectroscopy is one of the most valuable tools in the analysis of polymers [1] providing information about the chemical composition. In order to gain information about their structure polarized infrared spectroscopy can be applied.

Usually a polymer is amorphous and lacks long-range order. The polymeric chains form a random network as depicted in figure 2.1 which is obtained by covalent bonds between chains known as cross linking or end linking. This network is called elastomeric, because it consists of flexible chains permanently linked together by chemical crosslinks. Therefore polymers are composed of hard segment domains serving as crosslinks between the amorphous soft segment domains. The soft segments are mobile and normally present in coiled formation.

The polymer chains in this network can be ordered by means of heating and cooling which causes amorphous and crystalline areas. Stretching during the cooling process yields ordered polymer chains with orientation in one direction which gives a film of greater toughness and tensile strength. So polymers are also characterized by their degree of crystallinity, which becomes apparent in their optical properties. Polymer chains in a film can also become oriented to a certain degree by simply stretching it without a change in temperature, see figure 2.1. It shows a microscopic picture (c) of the measured film, whose thickness, approximately 27,5 μm , can be measured from picture (b) captured by an Optical Coherence Tomography (OCT)-system.

PLA is one of the most important ecologically beneficial biodegradable thermoplastic polyesters with extensive applications. It features renewable resources,

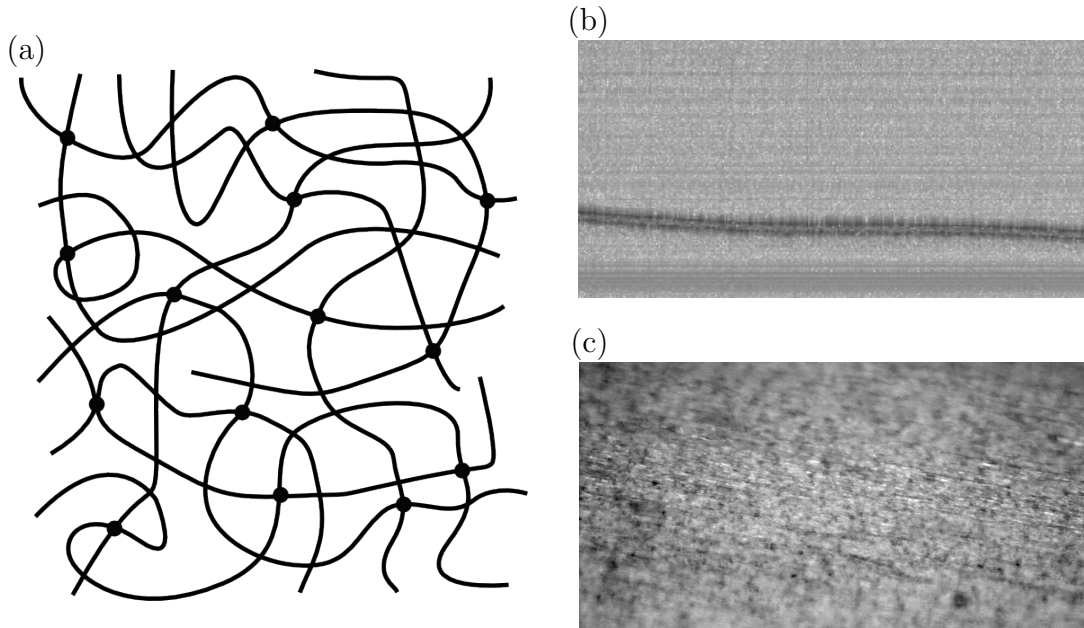


FIGURE 2.1: (a) Schematic representation of the morphological structure of an unstretched polymeric network. The points indicate the crosslinking between chains. The film thickness ($27,5 \mu\text{m}$) can be estimated with the help of picture (b) recorded by an OCT-system at Recendt. The uniaxial orientation of a stretched PLA film can be seen in picture (c) by microscopic magnification ($\times 100$).

low toxicity and the desirable characteristic to decompose into naturally occurring metabolites via hydrolysis or enzymatic processes, along with performance comparable with many petroleum-based plastics [2]. Its biocompatibility makes PLA a natural choice for biomedical applications. The basic building block of PLA is the lactic acid obtained from bacterial fermentation of sugars extracted primarily from corn starch or sugar cane. Lactic acid also known as milk acid is the most widely occurring carboxylic acid in nature. Ring-opening polymerization, see figure 2.2, of lactic acid cyclic dimer known as lactide, initiated by a catalyst, results in PLA with controlled molecular weight.

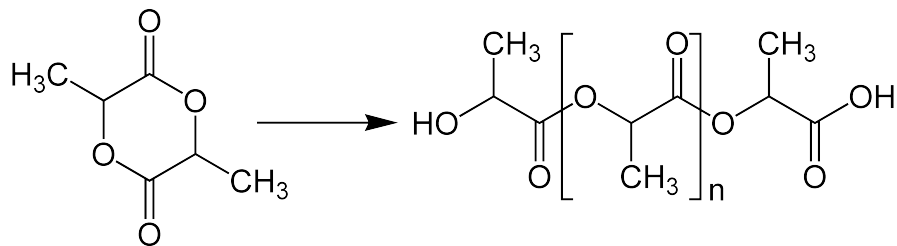


FIGURE 2.2: PLA synthesis by ring-opening polymerization. Image taken from Wikipedia⁴.

Pure PLA has many limitations such as brittleness, low impact strength, low ability in resisting thermal deformation and slow degradation rate. In order to

⁴<http://de.wikipedia.org/wiki/Polylactide> (last visited October 30, 2012)

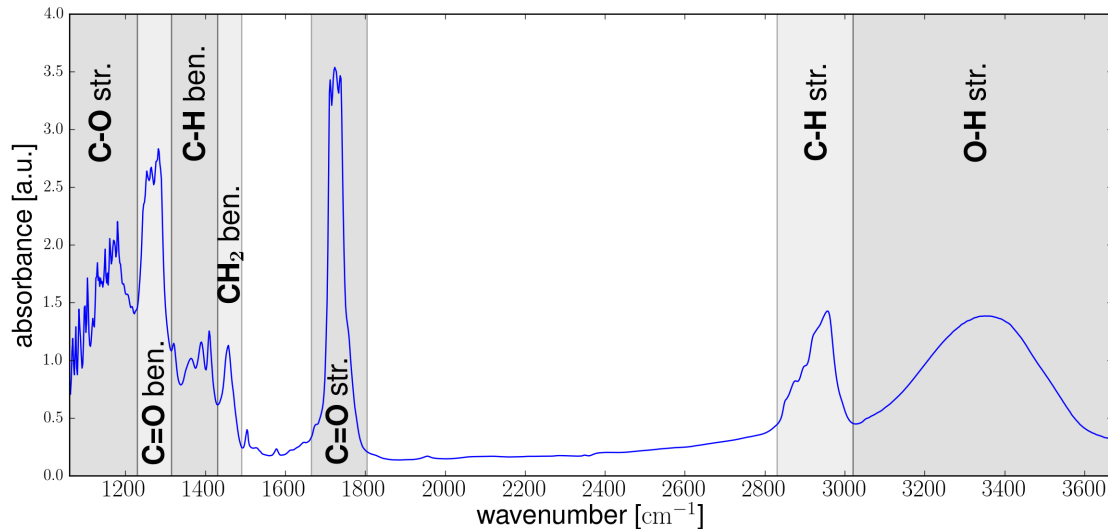


FIGURE 2.3: Mid-infrared spectrum with the assigned vibrational modes - stretching (str.) and bending (ben.) - of the functional groups of the PLA film.

improve crystallinity, thermal stability and mechanical properties PLA is incorporated with other synthetic polymers or mixed with fillers and plasticizers. Thus in order to entirely determine the composition of an unknown bioplastic product such as the biodegradable bag bought in a supermarket from which the PLA film samples were cut out and used for measurement in this work, is a difficult task going beyond the scope of this thesis and will therefore only be estimated here. FTIR spectroscopy, described in the next section 2.2, has been used extensively for PLA studies for its high sensitivity and low cost. The instrumentation is readily available allowing in-line measurements during film processing as well as in situ monitoring of polymerization reactions [3].

In figure 2.3 the absorbance spectrum of the PLA film is shown and the functional groups corresponding to certain mid-infrared wavenumber regions are identified. The important wavenumber region in order to characterize crystallinity is between 1300 and 1150 cm⁻¹ assigned to C-H bending, C=O bending and C-O stretching vibrations. In low molecular weight samples these regions, also known as crystalline bands [4], can be absent indicating a low degree of crystallinity. Furthermore the PLA spectrum contains characteristic absorption bands at approximately 1450 cm⁻¹ assigned to the methylene bending mode and the sharp absorption peak at approximately 1750 cm⁻¹ associated with the C=O stretching vibration. The magnitude and form of the two broad absorption bands at higher wavenumbers, namely the C-H stretching vibration at 2800-3000 cm⁻¹ and the hydroxyl band centered at about 3400 cm⁻¹, indicate the modification of the PLA film with plasticizers [5].

2.2 FTIR Spectroscopy

The name FTIR spectroscopy highlights directly the mathematical operation used to calculate the spectrum after the light was modulated by an interferometer and thus it indicates the difference in comparison to dispersive spectrometers using grating monochromators or prisms. It is common to only use the abbreviation FTIR when speaking of the method. FTIR spectrometers have been commercially available for about 40 years and have replaced dispersive devices in the course of time. As FTIR is the standard method in infrared spectroscopy it would not be necessary to emphasize the FT-term. The advantages of FTIR compared to dispersive spectrometers revolutionized the measurement of infrared spectra and made FTIR spectrometers a device to be found in almost every analytical chemistry laboratory nowadays.

2.2.1 IR Spectroscopy

The infrared region of the electromagnetic spectrum follows the visible spectrum with increasing wavelength and decreasing frequency and is divided into three regions: the near-, mid- and far- infrared, named for their relation to the visible spectrum, see table 2.1. The wavelength λ and the frequency f are connected via the speed of light $c = \lambda f$.

NIR	MIR	FIR
12500 - 4000 cm^{-1}	4000 - 400 cm^{-1}	400 - 10 cm^{-1}
0,8 - 2,5 μm	2,5 - 25 μm	25 - 1000 μm

TABLE 2.1: The three regions of the infrared spectrum in terms of wavenumber and wavelength according to DIN 5031

In infrared spectroscopy the spectrum is presented in terms of the wavenumber ν in units of cm^{-1} . This is the number of waves within a length of one centimeter and is given by $1/\lambda$. This unit has the advantage of being linear with the photon energy $E = hf$, h being the Planck constant⁵. The interaction of light and matter causes very different processes depending on the wavelength. Whereas in the visible and in the ultraviolet region the photons have enough energy to cause electron transitions, the quantum energy of infrared photons is in the range 0,001 to 1,6 eV⁶ which corresponds to energies separating the quantum states of molecular vibrations.

So the absorption of infrared radiation causes transitions between molecular vibrational energy levels. In order to transfer energy from the infrared photon to the molecule via absorption, the molecular vibration must cause a change in the dipole moment of the molecule. This is known as the selection rule for infrared absorption and determines if a molecule is infrared active. The infrared activity depends on the symmetry of the molecule, which also determines the possible

⁵ $h = 6,62607 \cdot 10^{-34} \text{ J s}$

⁶ 1 electron volt is given by $1\text{eV} = 1,60218 \cdot 10^{-19} \text{ J}$

vibrational modes. Polyatomic molecules containing N atoms have $3N$ degrees of freedom, which are subdivided into translational, rotational and vibrational degrees of freedom as shown in table 2.2. In addition modes can have the same frequency and are then called degenerate.

Type of degrees of freedom	Linear	Non-linear
Translational	3	3
Rotational	2	3
Vibrational	$3N-5$	$3N-6$
Total	$3N$	$3N$

TABLE 2.2: Degrees of freedom of polyatomic molecules

The harmonic oscillator provides a demonstrative model which considers the chemical bonds as springs between the atoms. The electromagnetic field causes the periodical displacement. The frequencies of the molecular vibrations depend on the masses of the atoms, their geometric arrangement, and the strength of their chemical bonds. The potential energy is then a function of the displacement from the equilibrium positions of the atoms. If the vibrational modes were strictly harmonic, i.e. obeying Hooke's law, overtone and combination bands would not be allowed. For a more realistic description anharmonicity has to be introduced [6].

Overtone bands take place at multiples of the fundamental absorption frequency. Combination bands are observed when two or more fundamental vibrations are excited simultaneously. Overtone and combination bands take place in the NIR-region and are usually much weaker than the fundamental modes from which they are derived. The fundamental modes are found in the MIR-region and are indicative of specific chemical functional groups in the molecule. Below 1500 cm^{-1} and especially in the FIR-region skeletal modes become possible and whole molecules oscillate. This region usually contains very complicated series of absorption bands and it is much more difficult to pick out individual bands. Because of the unique patterns found there, which allow the identification of molecules, it is often called the fingerprint region.

An infrared spectrum is commonly obtained by passing infrared radiation through a sample and determining what fraction of the incident radiation is transmitted⁷ at a particular energy. This fraction is defined as the ratio of the spectrum of the sample and the background spectrum. It is called the transmission $T = I/I_0$, which yields the fundamental law of quantitative spectroscopy, the Beer-Lambert-law [6]:

$$A = -\log_{10} T = \varepsilon l \tilde{c} \quad (2.1)$$

The law defines the dimensionless absorbance A as the negative decadic logarithm of the transmission and relates the absorption of light to the properties of the material, where ε is the molar absorptivity in units of m^2/mol and \tilde{c} is the molar concentration in units of mol/m^3 . The absorbance is apparently proportional

⁷In infrared transmission spectroscopy the scattered and reflected light is generally disregarded, but can be estimated.

to the thickness of the sample given by l and directly proportional to the concentration of the absorbing material in the sample. That is why the absorbance is a very significant and favoured quantity for describing a material in infrared spectroscopy.

The infrared spectrum of a given molecule is unique and can be used to identify that molecule. In order to extract structural information from a spectrum it is useful to consult correlation tables, which link the functional groups to the particular absorption bands. For example, the correlation table for polymers shown in figure 2.4 helped to interpret the spectrum of the sample used for this thesis. The easier way is using a software which compares the spectra of unknown materials to a large number of reference spectra in a database.

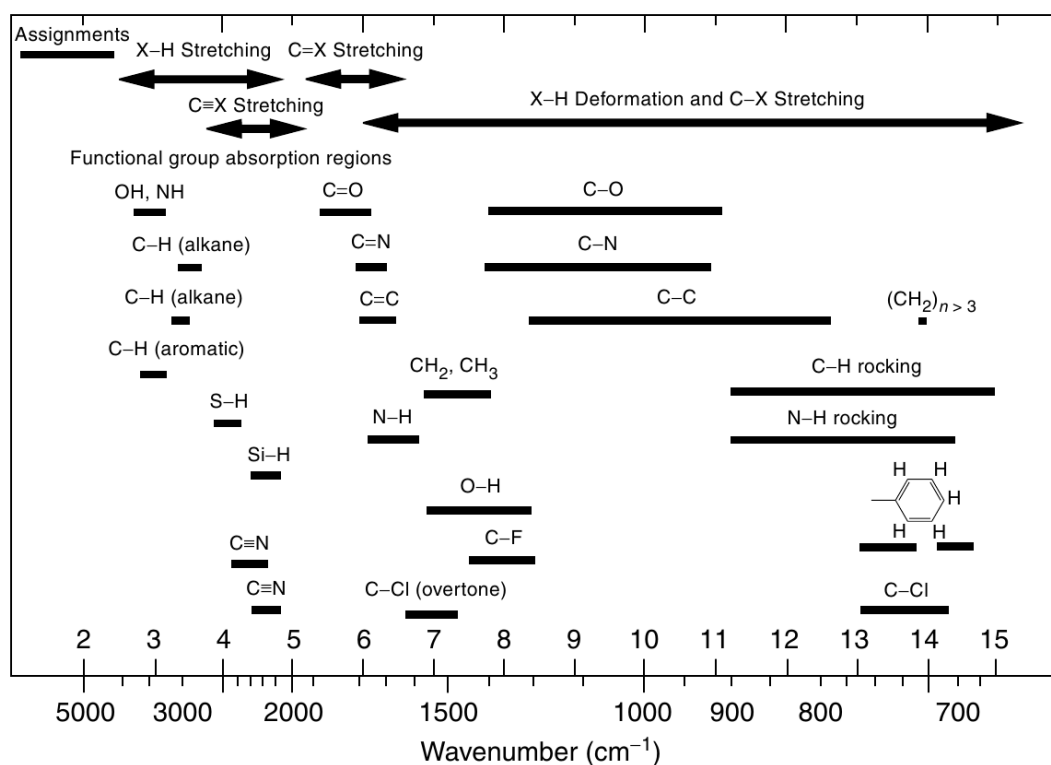


FIGURE 2.4: Correlation table for infrared bands of polymers. Image taken from reference [7].

2.2.2 Principles of FTIR

The essential piece of every FTIR spectrometer is the Michelson interferometer designed by Michelson in 1891. The most important component apart from the optics is a computer dealing with data processing. To understand FTIR spectroscopy it is necessary to understand the functionality of the interferometer and the task done by the computer.

In the interferometer a beam from a broadband infrared source is divided by a beamsplitter into two optical paths and then recombined after a path difference δ has been introduced. This path difference varies periodically as the optical path

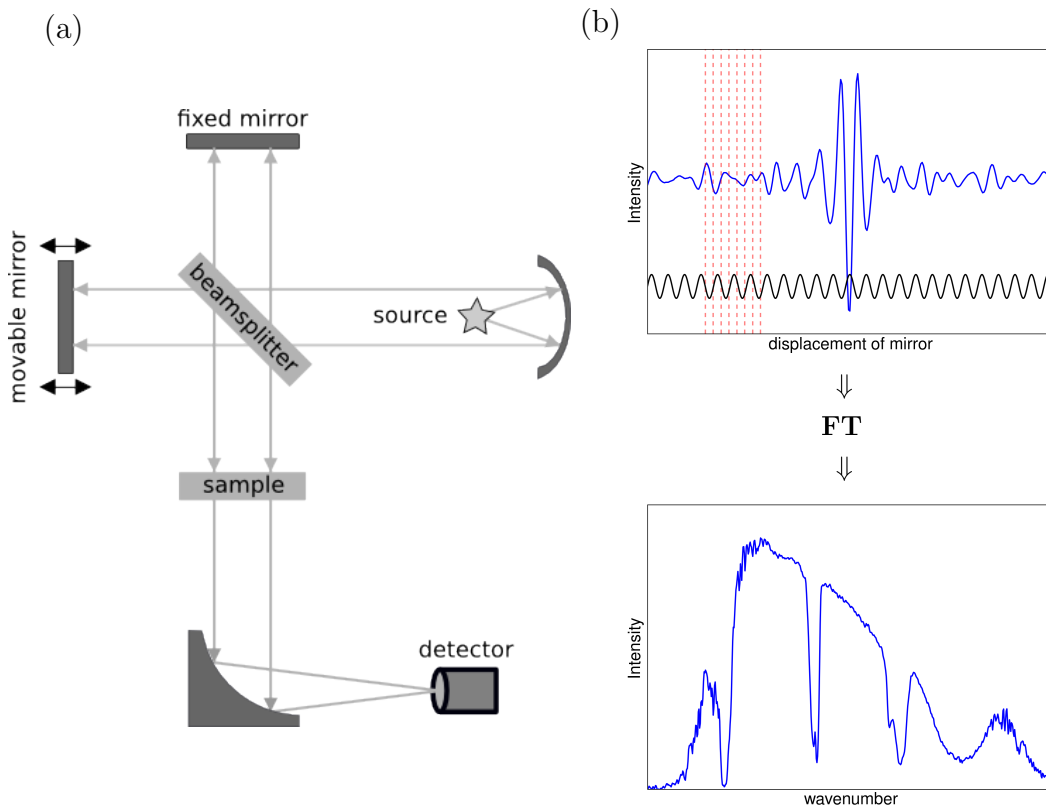


FIGURE 2.5: (a) Schematic representation of the beam trajectory in FTIR spectroscopy. At the top of (b) the detector signal (blue) and the interferogram generated by the HeNe laser (black) as a function of the mirror displacement is depicted. The zero crossings of the laser interferogram define the positions where the interferogram is sampled (red dashed lines). The Fourier transformation (FT) of the blue interferogram delivers the spectrum at the bottom of (b).

length of the light in one arm of the interferometer is modulated through a movable mirror, which moves forward and backward at a given velocity, whereas the optical path length of the light in the other arm remains unaffected, because it is reflected by a fixed mirror, see figure 2.5. The measured power $I(\delta)$ at the detector is produced by the interference of the two reunited beams dependent on the displacement of the movable mirror as stated in equation 2.2. At zero path difference position, when the two mirrors are optically equidistant from the beamsplitter, the intensity is at its maximum, because all wavelengths of the light source interfere constructively. When a path difference is introduced some wavelengths interfere constructively, whereas others interfere destructively at a specific point, producing a positive or a negative peak dependent on the wavelengths and their heights also on the amplitudes of the interfering waves. From the interference pattern the spectrum of the light source can be extracted through Fourier transformation. For the analysis of a sample the beam is transmitted through or reflected by the material of interest, and the spectrum of the sample is then compared to the background spectrum of the source. By this means absorbance spectra can be computed, which is widely used for material characterization.

The accuracy of the Fourier transformation of $I(\delta)$ depends on recording the

signal at equally spaced mirror positions. Otherwise incorrect spectral features, often called spectral artefacts, would arise. Considering environmental influences and fluctuations it is technically difficult to move the mirror at a constant velocity. For this reason a Helium-Neon laser beam with $\lambda = 633$ nm traverses the same optical path as the infrared light to monitor the mirror position. Measuring this position allows to record the interferogram directly as a function of the spatial coordinate δ . The monochromatic laser light generates a sine-squared interferogram pattern, shown in figure 2.5(b), with a constant frequency and amplitude. Each time the interferogram of the laser is passing zero, the analog-to-digital converter (ADC) is triggered to simultaneously digitize the infrared light intensity registered at the detector. As a result the digital interferogram is obtained, actually a digital point-by-point plot of intensity versus mirror position. For a monochromatic light source the interferogram is given as:

$$\tilde{I}(\delta) = \frac{1}{2} \tilde{S}(\nu) \cos\left(2\pi \frac{\delta}{\lambda}\right) \quad (2.2)$$

where $\tilde{S}(\nu)$ is the spectrum, which in the monochromatic case consists of a single wavenumber argument. Each time the path difference reaches a multiple of the wavelength the intensity reaches its maximum. The factor 1/2 comes from neglecting the constant component of the signal passing the beamsplitter without any modulation [6]. The inclusion of some wavenumber-dependent factors affecting the magnitude of the signal, such as the nonideality of the beamsplitter, the detector response and the amplifier characteristics, to the formula of the interferogram, yields the modified equation:

$$I(\delta) = S(\nu) \cos 2\pi\nu\delta \quad (2.3)$$

where the generalized spectrum $S(\nu)$ contains these factors, which remain constant throughout the measurement. In order to see the influence of the velocity V of the mirror, the path difference given by $\delta = 2Vt$ can be inserted in 2.3 and results in a time-dependent signal:

$$I(t) = S(\nu) \cos(2\pi\nu \cdot 2Vt) \quad (2.4)$$

This equation describes the interferogram in time-domain, where the factor $f_\nu = 2V\nu$ represents the frequency of the interferogram corresponding to the wavenumber ν . It is important to notice the fact that each wavenumber is modulated with a different frequency and the Fourier transformation of equation 2.4 would directly extract f_ν of each wavenumber. When finally a lightsource with a continuous spectrum is included in the mathematical formulation, the interferogram is given by:

$$I(\delta) = \int_{-\infty}^{\infty} S(\nu) \cos 2\pi\nu\delta \, d\nu \quad (2.5)$$

In order to determine the wavenumber components making up the interferogram, it can be converted from the spatial domain via a cosine Fourier transformation,

which yields the spectrum:

$$S(\nu') = \int_{-\infty}^{\infty} I(\delta) \cos 2\pi\nu'\delta \, d\delta \quad (2.6)$$

Measuring a spectrum means dealing with a digitized interferogram consisting of N discrete, equidistant points as mentioned above. Thus actually the discrete Fourier transformation (DFT) has to be used which leads to a discrete spectrum:

$$S(k \cdot \Delta\nu) = \sum_{n=0}^{N-1} I(n \cdot \Delta x) \exp(i2\pi nk/N) \quad (2.7)$$

where the continuous variables δ and ν have been replaced by $n \cdot \Delta x$ and $k \cdot \Delta\nu$. The spacing between two measurement points denoted as Δx is given by half of the laser wavelength. The variable k also runs from 0 to $N-1$. $\Delta\nu$ is the spacing in the spectrum and determines the resolution of the spectrum. It is related to Δx by:

$$\Delta\nu = \frac{1}{N \cdot \Delta x} \quad (2.8)$$

The error in $\Delta\nu$ is of the same order as in Δx , solely determined by the precision of the very stable laser wavelength which results in a wavenumber calibration of high precision, also known as the Connes advantage. The equation 2.8 determines a limit for the spectral resolution as the inverse of the achievable optical path difference. In order to resolve two spectral lines separated by a distance $\Delta\nu$ the interferogram has to be measured up to a path length of at least $1/\Delta\nu$. By means of the inverse discrete Fourier transformation the interferogram can easily be reconstructed:

$$I(n \cdot \Delta x) = \frac{1}{N} \sum_{k=0}^{N-1} S(k \cdot \Delta\nu) \exp(-i2\pi nk/N) \quad (2.9)$$

For $n = 0$ the equation states that the intensity measured at the interferogram centerburst is equal to the sum of all N spectral intensities divided by N . So the height of the centerburst gives the average spectral intensity. The discrete Fourier transformation must be calculated numerically by a computer, which uses an efficient algorithm called the Fast Fourier transformation (FFT). The quality of the software directly determines the accuracy of the spectra, see section 2.2.3.

The quality of optical measurements is often characterized by the signal-to-noise ratio (SNR), which may be limited either by optical noise or by detector noise. For FTIR spectroscopy in the mid-infrared region the detector noise exceeds all other noise sources. The SNR of a spectrum is given by [6]:

$$\text{SNR} = \frac{S'}{N'} = \frac{U_\nu(T) \Theta \Delta\nu \sqrt{t} \xi}{\text{NEP}} \quad (2.10)$$

where S' is the power transmitted to a detector through an interferometer at a resolution $\Delta\nu$ and operating at a throughput Θ with an efficiency ξ . $U_\nu(T)$ is the

spectral energy density at wavenumber ν from a blackbody source at temperature T , described by Planck's law. The noise power N' is given by the noise equivalent power (NEP) of the detector measured in $\text{W} \cdot \text{Hz}^{-1/2}$ and depends on the measurement time t .

Relationships between the entities of equation 2.10 deliver important pieces of information for practice. For example, increasing the measurement time by a factor of two, by either averaging of two spectra or acquiring a spectrum at halved mirror velocity, results in an improvement of the SNR by a factor of $\sqrt{2}$. Otherwise the enhancement of spectral resolution at a constant mirror velocity and measurement time decreases the SNR. In order to compensate a twofold enhancement the measurement time must be increased four times. Thus a better resolution is achieved at a very high cost due to reduction of the SNR. In order to achieve an optimal performance the resolution is set to be equal or slightly smaller than the expected width of the most narrow feature on the collected spectrum.

In addition to the Connes advantage, already mentioned above, resulting in a much higher resolution than dispersive instruments would provide, the two most important advantages of FTIR result in a higher SNR and can be stated as:

- *The Fellgett or Multiplex advantage:*
In FTIR spectrometers all wavelengths are measured simultaneously offering identical conditions for each wavelength. This results not only in short measurement times but especially in a relative improvement in SNR of the order of \sqrt{N} , where N is the number of sample points comprising the spectrum.
- *The Jacquinot or Throughput advantage:*
The circular apertures used in FTIR spectrometers have a larger area than the linear slits used in grating spectrometers, thus enabling higher throughput of radiation.

2.2.3 FTIR Data Processing

In order to describe the detector signal as spectrum of the light source, an ADC has to digitize the analog signal and send it to a software which has to produce a meaningful spectrum out of it. The digitalization process is characterized by the sampling rate f_s , which is the number of samples per unit of time taken from a continuous signal to make a discrete signal. This frequency is determined by the Nyquist criterion, which defines the highest frequency that can be recorded at a given sampling rate in order to be able to fully reconstruct the signal without aliasing effects. In FTIR spectroscopy this leads to the Nyquist wavenumber, which is one half of the HeNe laser wavenumber. So the sampling rate can be adjusted through the velocity of the movable mirror, see equation 2.4, and determines the maximum wavenumber recordable.

The task of the software in the course of the data manipulation is to accommodate instrumental imperfections and basic scan limitations before the DFT can be applied. The resolution of a spectrum is determined by the distance that the moving mirror travels, but as can be seen in equation 2.6 the limits of integration would require infinite mirror displacement neglecting the finite coherence length.

As effect of measuring the signal over a limited retardation it causes an abrupt truncation at finite optical path difference and thus a leakage of the spectral intensity in the side lobes of the interferogram. It is impossible to move the mirror over infinite distances, and consequently equation 2.6 must be rewritten:

$$S_f(\nu) = \int_{-\infty}^{+\infty} I(\delta) T(\delta) \cos 2\pi\nu\delta \, d\delta \quad (2.11)$$

where $S_f(\nu)$ represents the spectrum of a finite interferogram and $T(\delta)$ is denoted as an apodization function, which is usually a continuous function of δ and brings the interferogram smoothly down to zero at the edges of the sampled region, attenuating the spurious side lobes. The finite Fourier transformation of an apodization function is called the Instrument line shape (ILS) function illustrating the influence of the instrument respectively the spectrometer. The spectrum $S_f(\nu)$ can thus be obtained by convolving $S(\nu)$ corresponding to infinite optical path difference with the ILS function:

$$S_f(\nu) = S(\nu) * \text{ILS}(\nu) \quad (2.12)$$

The convolution of two functions $f * g$ is the product of the Fourier transform of the functions f and g and defined as:

$$(f * g)(x) = \int_{-\infty}^{+\infty} f(y)g(x - y)dy \quad (2.13)$$

There exist several popular apodization functions used in FTIR spectroscopy leaving the choice to the user. But it is important to mention that the leakage reduction is only possible at the cost of resolution, dependent on the apodization function used. A detailed discussion of the effect of apodization functions can be found in [6] or [8].

Influences such as bad mirror alignment and beam divergence resulting in mirror asymmetries along with other optical or electronic imperfections as wavenumber-dependent phase delays of the detector, the amplifier or the electronic filters can cause erroneous readings of various spectral components. When the position of zero path difference is not properly sampled, the Fourier transformation of a measured interferogram yields a complex spectrum with out-of-phase components which has to be corrected by a method moving the components of the spectrum that are located in the imaginary domain to the real domain. In this thesis the phase correction is accomplished by the Mertz method, described in appendix B.

The interferogram usually varies around a constant value called the baseline. The sample can cause an altering of the baseline mainly because of wavenumber-dependent effects such as scattering and reflection resulting in the need of another data manipulation procedure called baseline correction.

In order to provide a larger number of data points a process called zero filling can be performed simply by means of the addition of zeros to the end of an interferogram, which is an accurate form of interpolation. The zero filling factor determines the number of zeros, which are added only as a multiple of the data

points of the interferogram. It should be noted that zero filling does not introduce any errors because the ILS function is not changed.

2.3 Polarization of Light

Polarization is a property of light which is often disregarded because for human eyes it is not directly visible and the light from familiar sources such as the sun is unpolarized. Materials can show per se or can be modified to show, for example by means of mechanical stress, polarizing effects like birefringence, dichroism or optical activity. Each interaction of light and matter, namely reflection, transmission, refraction and scattering, can affect the state of polarization, whereas the reason for a change can be very different each time.

The time-varying orientation of the electric field strength \mathbf{E} is chosen to define the state of polarization of an electromagnetic wave in vacuum. Once the polarization of \mathbf{E} has been determined, the polarization of the three remaining vectors describing light, namely the electric displacement vector \mathbf{D} , the magnetic field vector \mathbf{H} , and the magnetic induction vector \mathbf{B} , can be found by Maxwell's field equations and the associated constitutive relations.

The different states of polarization of fully polarized and monochromatic radiation are elliptical, linear and circular polarization. In order to describe these states and the polarizing effects of optical devices or the sample, matrix methods are convenient. It is important to mention, that the measurable intensities of light refer to a superposition of many millions of waves with different orientations. Thus even monochromatic laserlight can actually only be partially polarized and is characterized by the degree of polarization. The Stokes formalism represented in terms of intensities is accounting for this fact and by means of the four Stokes polarization parameters any state of polarized light can be completely described. The Jones calculus, see appendix A, represented in terms of electric fields, is not capable of describing partially polarized light, however this matrix formalism is easier to interpret and is used throughout this thesis. By means of the coherency matrix, see reference [9], consisting of time averaged electric field components, the degree of polarization can also be considered, for definition see reference [10].

2.3.1 Birefringence and Dichroism

When light interacts with an insulting, isotropic, linear material the electric field induces a local electric dipole moment by exerting a force on the bound charges and slightly separating them. The constitutive relation describing the electric field in the isotropic material is given by:

$$\mathbf{D} = \varepsilon_0 \varepsilon \mathbf{E} \quad (2.14)$$

where ε_0 is the vacuum permittivity and ε is the relative permittivity of the material, which may be dependent on the location in the material, but also on the frequency of the light, showing dispersion. Furthermore the permittivity can depend on the strength of the electric field in a nonlinear medium and depends on

the direction of the electric field becoming a tensor in anisotropic materials. This can be written using Einstein summation convention:

$$\mathbf{D}_i = \varepsilon_0 \varepsilon_{ij} \mathbf{E}_j \quad (2.15)$$

So the relative permittivity provides all electrical information about a material making it to a significant quantity, which is also related to the refractive index $n = \sqrt{\varepsilon}$ at light frequencies. Classically n is defined as the factor by which the vacuum wavelength λ_0 and the vacuum velocity c_0 of the radiation are reduced by propagation in a medium, where the velocity is given by $c = c_0/n$ and the wavelength is given by $\lambda = \lambda_0/n$. The dielectric tensor is symmetric, $\varepsilon_{ij} = \varepsilon_{ji}$, so it is always possible to find a set of coordinate axes, called the principal axes, causing the off-diagonal terms in equation 2.15 to become zero and the tensor to become diagonalized. This yields:

$$\begin{pmatrix} D_x \\ D_y \\ D_z \end{pmatrix} = \varepsilon_0 \begin{pmatrix} n_x^2 & 0 & 0 \\ 0 & n_y^2 & 0 \\ 0 & 0 & n_z^2 \end{pmatrix} \begin{pmatrix} E_x \\ E_y \\ E_z \end{pmatrix} \quad (2.16)$$

where n_x , n_y , and n_z are the principal indices of refraction. \mathbf{E} and \mathbf{D} are parallel for waves propagating along these particular directions. If the three principal refractive indices are different, the material is termed biaxial, and if two indices are equal, it is called uniaxial. In cubic materials all three indices are equal and the medium is optically isotropic. A useful geometrical representation of the refractive index being actually a symmetric tensor of second-rank is the index ellipsoid also called the optical indicatrix, shown in figure 2.6, where the length of the semi-axes are the principal refractive indices.

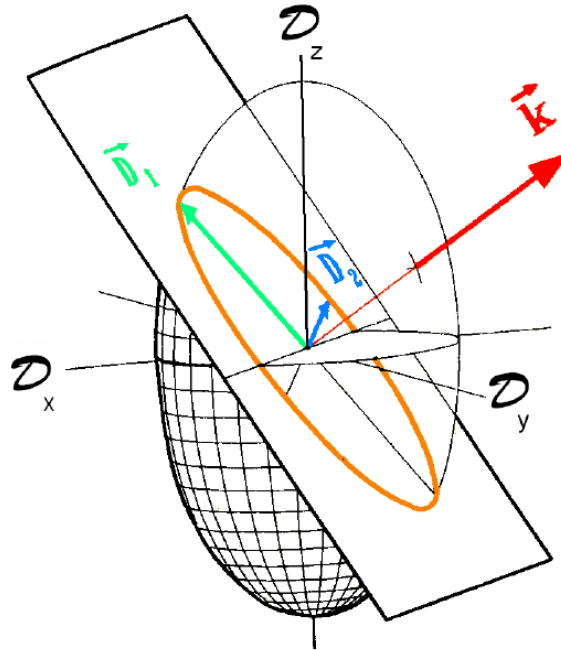


FIGURE 2.6: Index ellipsoid in \mathbf{D} -space. Image adapted from reference [11].

Considering the general case of a plane wave travelling in an anisotropic material in an arbitrary direction defined by its wavevector \mathbf{k} , the effective refractive indices related to this direction can be determined by cutting the indicatrix by a plane perpendicular to the propagation direction going through the origin of the indicatrix. This procedure delivers the index-ellipse yielding the eigendielectric displacements \mathbf{D}_1 and \mathbf{D}_2 as the principal axes and the refractive indices n_1 and n_2 as their lengths. The two wave components along these directions travel at different phase velocities, c_0/n_1 and c_0/n_2 , and they therefore undergo different phase delays, which yields a phase retardation $\Delta = \delta_2 - \delta_1 = \Delta n k_0 d$ after propagating a distance d , where k_0 is the angular wavenumber of vacuum given by $k_0 = 2\pi/\lambda_0$, and $\Delta n = n_2 - n_1$ defines the birefringence.

The different refractive indices cause, as the name implies, the two polarization components to be refracted in different directions dependent on the angle of incidence with respect to the principal axes. At normal incidence parallel to a principal axis the two components do not separate spatially and only the phase difference is evident, which describes the principle of operation of a phase retarder and can be expressed by means of its Jones matrix:

$$\begin{bmatrix} 1 & 0 \\ 0 & \exp(-i\Delta) \end{bmatrix} \quad (2.17)$$

So if the refractive index depends on the polarization state and propagation direction of light, birefringence, also called double refraction, takes place. Many plastics show birefringence, because their individual chains become oriented in particular directions when the plastic is molded or extruded. Furthermore the orientation in polymers can simply be affected by stretching, as mentioned above, also resulting in birefringence. For rubber-elastic materials the degree of orientation is directly proportional to the applied stress σ and the birefringence is directly proportional to the orientation, which yields for uniaxial tension:

$$\Delta n = C_\sigma \sigma \quad (2.18)$$

where C_σ is the stress optical coefficient dependent on the temperature and the chemical structure of the material. The proportionality between the birefringence and an applied stress is generally known as the photoelastic effect.

In order to describe light absorption by media the extinction coefficient κ has to be introduced as imaginary component of the complex refractive index [12]:

$$\tilde{n} = n - i\kappa \quad (2.19)$$

The real part of the refractive index n relates to the phase velocity, while the imaginary part κ indicates the amount of absorption loss when the electromagnetic wave propagates through a material. Thus in an anisotropic absorbing material, such as a stretched polymer film or a wire grid polarizer, the absorption can also depend on the polarization state of light which is called dichroism.

This directional absorption makes infrared spectroscopy very useful to study molecular orientation and can be analyzed by measuring spectra using light linearly polarized parallel and perpendicular to a fixed reference direction, respectively.

This type of experiment is called infrared linear dichroism (IRLD) [13]. The two parameters commonly used to characterize linear dichroism are the dichroic ratio:

$$R = \frac{A_p}{A_s} \quad (2.20)$$

and the dichroic difference:

$$\Delta A = A_p - A_s \quad (2.21)$$

where A_p and A_s are the absorbances measured with light polarized parallel and perpendicular to the reference direction, respectively. The difference between the absorption of the two polarization components is often extremely small and requires a high signal-to-noise ratio. The static measurement method can be improved by means of polarization modulation, which makes it possible to measure the two absorbances simultaneously.

2.3.2 Polarization Modulation

The state of polarization may be modulated by simply rotating a polarizer, which is a common method in ellipsometry [14], but lacks the opportunity of real-time spectroscopic measurements because of the limited velocity of the rotation. For the measurements in this work the polarization modulation, also called phase modulation⁸, is achieved by a photoelastic modulator (PEM).

The PEM makes use of the photoelastic effect, which causes birefringence in an isotropic material induced by the application of mechanical stress, at which the magnitude of the birefringence is directly proportional to the stress. Piezoelectric transducers bonded to the optical element transform an applied AC voltage into mechanical oscillation causing a standing sound wave at resonant frequency in the optical element, and the indices of refraction along the orthogonal stress axes of the PEM begin to vary in a sinusoidal manner. If linearly polarized light oriented at 45° with respect to the stress axes enters the PEM, the phase difference between the two components of the polarized light along these axes becomes periodically modulated and can be stated as:

$$\phi = \phi_0 \sin(\omega_m t) \propto \frac{V_m}{\lambda} \sin(\omega_m t) \quad (2.22)$$

where ω_m is the angular frequency of the PEM and ϕ_0 , being the amplitude of the modulation, denotes the maximum phase difference apparently dependent on the wavelength respectively wavenumber of the incident radiation. By means of the voltage V_m applied to the piezoelectric transducers the peak retardation $\phi_0(\nu)$ can be adjusted for specific wavenumbers. The behavior of the output beam can be seen in figure 2.7, where the polarization states during one modulation period with peak retardation $\phi_0 = \pi$ are depicted. At two times during one period the phase difference is zero and the linearly polarized light is unmodified. The same happens, when ϕ is $\pm\pi$ at the peaks of the retardation, producing also linearly polarized light, but in the perpendicular direction of the incident light. Thus the

⁸Actually the phase difference of the two polarization components is modulated.

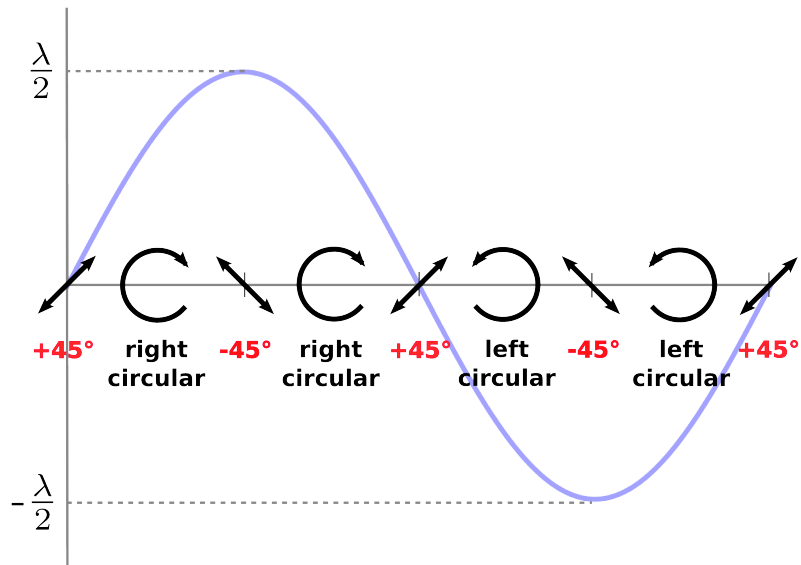


FIGURE 2.7: Schematic representation of the polarization states during one modulation period. The y-axis represents the phase difference according to equation 2.22. Image redrawn after reference [15].

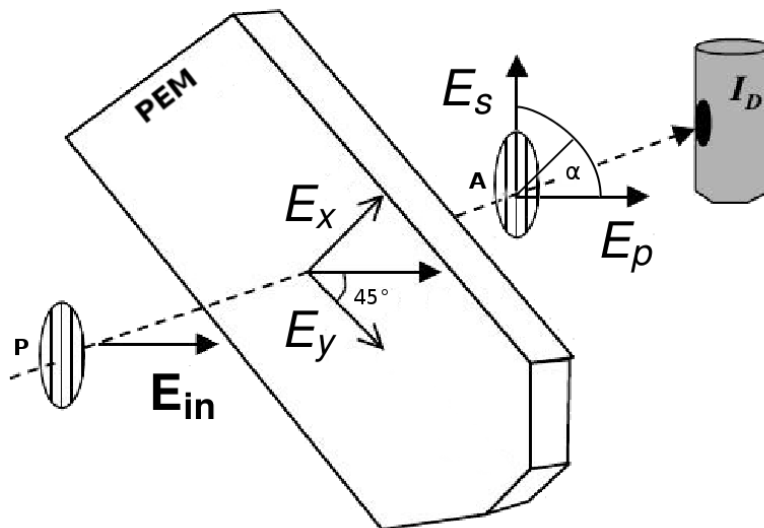


FIGURE 2.8: Optical configuration in order to measure the intensity modulation by the PEM. The angle α of the analyzer with respect to the PEM-coordinate system determines which polarization component is measured.

light beam is modulated between two orthogonal, linearly polarized states at twice the frequency of the PEM. For odd multiples of $\pi/2$ the light is circularly polarized and for other retardations the radiation is elliptically polarized.

Measuring a light signal always means to measure the intensity, which is given by the squared amplitude of the light wave cancelling out the phase. In order to recognize the phase modulation of the light the two polarization components parallel and perpendicular to the incident polarization direction \mathbf{E}_{in} have to be measured. This can be achieved with the optical setup shown in figure 2.8, where these two components are defined as E_p and E_s . At first the light passes the polarizer, directed at an angle of 45° with respect to E_x of the modulator, whose axes determine the coordinate system. Therefore the incoming electrical field is given by:

$$\mathbf{E}_{\text{in}} = R(-45) \begin{bmatrix} 1 & 0 \\ 0 & 0 \end{bmatrix} R(45) \mathbf{E}_0 = \begin{pmatrix} 1 \\ 1 \end{pmatrix} E_0 \quad (2.23)$$

where R denotes a rotation matrix, \mathbf{E}_0 is an arbitrary incoming electric field and E_0 is an arbitrary factor consisting of the components of \mathbf{E}_0 and constant factors arising from the calculation. The detected intensity $I(\alpha)$ is dependent on α , which is the angle of the analyzer inserted in front of the detector. If $\alpha = \pi/4$ (clockwise with respect to E_x) the component parallel to the incoming light E_p is measured and if $\alpha = -\pi/4$ the perpendicular component E_s is measured. The electric field at the detector is given by:

$$\mathbf{E}_{\text{out}} = \begin{bmatrix} \cos \alpha & \sin \alpha \\ -\sin \alpha & \cos \alpha \end{bmatrix} \begin{bmatrix} 1 & 0 \\ 0 & 0 \end{bmatrix} \begin{bmatrix} \cos \alpha & -\sin \alpha \\ \sin \alpha & \cos \alpha \end{bmatrix} \begin{bmatrix} 1 & 0 \\ 0 & \exp(i\phi) \end{bmatrix} \mathbf{E}_{\text{in}} \quad (2.24)$$

This yields the two intensity components, in p-direction:

$$I\left(-\frac{\pi}{4}\right) = I'_p = \frac{I'}{2}(1 - \cos \phi) \quad (2.25)$$

and in s-direction:

$$I\left(\frac{\pi}{4}\right) = I'_s = \frac{I'}{2}(1 + \cos \phi) \quad (2.26)$$

where I' consists of a constant factor accounting for the amplitude of \mathbf{E}_{in} , respectively the intensity of the incoming light.

According to the angle of the analyzer, either $-\pi/4$ or $\pi/4$, always one of the components, I'_p or I'_s , is zero. If there was no analyzer, the intensity at the detector I_D would become I' and no intensity modulation would be achieved, because:

$$I_D = I'_p + I'_s \quad (2.27)$$

If the incident radiation is polychromatic, it has to be considered that it is impossible to generate the same phase difference for all wavenumbers at the same time, because ϕ_0 is proportional to ν . In figure 2.9 at the top the intensity in p-direction, neglecting the constant term I' , can be seen for peak retardations varying around π during one modulation period. This shows the influence of polychromatic light, as the $\lambda/2$ -retardation is valid for only one wavenumber. At bigger wavenumbers the retardation becomes also bigger and at smaller wavenumbers the retardation

becomes smaller, which becomes noticeable in humps of the modulated intensity or respectively in an increase of the average intensity over the modulation cycles.

Furthermore it is important to notice that the modulation of the intensity and the polychromatic influence are very different in the two directions. The average of the intensity in p-direction becomes bigger at smaller wavenumbers, whereas this is exactly contrary in s-direction. The behavior of the average over one modulation cycle of the intensities is shown in figure 2.9 at the bottom. Thus calibration procedures are necessary to account for these effects, which will be described in section 3.1.3.

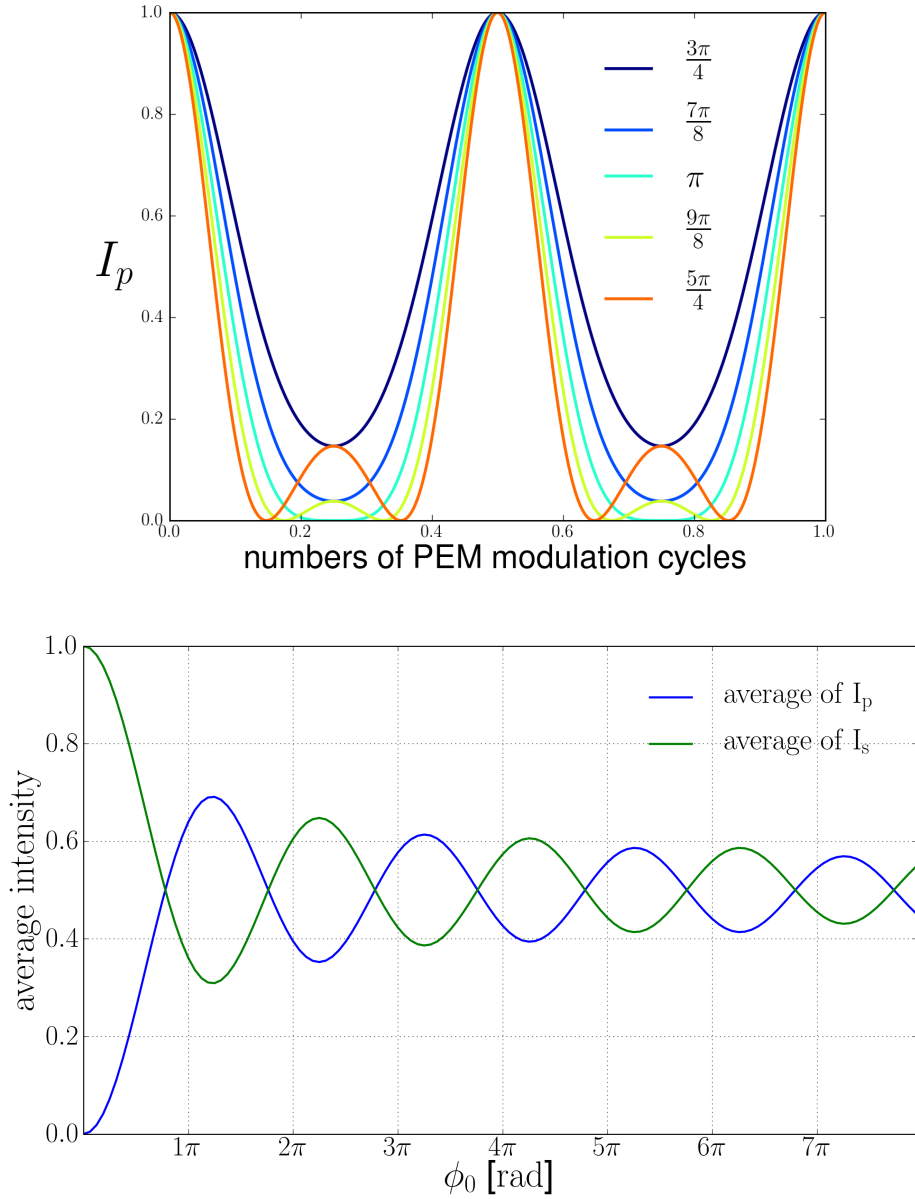


FIGURE 2.9: At the top the waveform of I_p with different peak retardations ϕ_0 according to the equation 2.25 is plotted. At the bottom the dependency of the average of the intensities I_p and I_s on the peak retardation is shown.

3. Methods and Materials

3.1 Methods

Polarized infrared spectroscopy delivers information about the composition of a material anyway, but crucially it offers information about the orientation of individual molecules. The modification of the amplitude or of the phase of the polarization components evoked by the sample provides the important information. Polarized infrared spectroscopy can be carried out either by means of static measurements, during which the polarization state of the incident light is kept constant, usually resulting in the need of changing the polarization state after each measurement, or by polarization-modulated measurements, which make it possible to deliver the phase and amplitude of the polarization components separately by a single measurement.

3.1.1 Phase-modulated IRLD

By means of IRLD experiments only the change in the amplitudes of the polarization components, actually the directional absorptions respectively the dichroism of a material, is measured. Static IRLD is straightforward the sequential recording of two spectra with linearly polarized light parallel and perpendicular to the reference direction to obtain the absorbances A_p and A_s . This process requires some time during which environmental fluctuations can cause low sensibility, making the determination of small dichroic effects impossible. Phase-modulated IRLD (PMIRLD) overcomes this problem by measuring the two absorbance components simultaneously. The optical configuration of PMIRLD is given by:

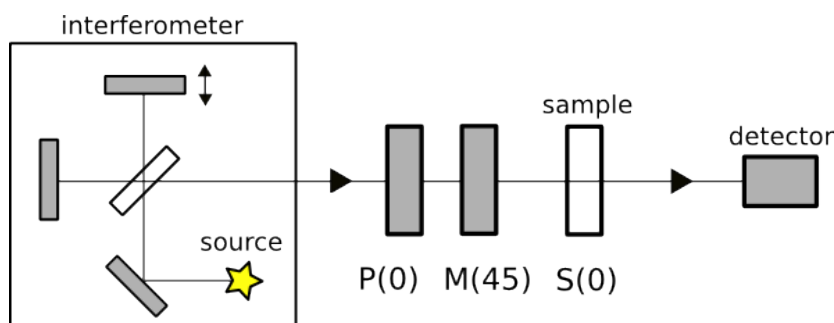


FIGURE 3.10: M indicates the modulator rotated at an angle of 45° related to the axis of the polarizer P. The sample-matrix S is not rotated.

This configuration is similar to the configuration in figure 2.8 with the only difference that a sample instead of an analyzer is inserted in the optical path.

According to the equations 2.25, 2.26 and 2.27 this yields the detected signal:

$$I_D(\nu, \phi) = \frac{I_p(\nu) + I_s(\nu)}{2} + \frac{I_p(\nu) - I_s(\nu)}{2} \cos \phi \quad (3.28)$$

where I' from the mentioned equations becomes I_p in p-direction and I_s in s-direction accounting for the fact that the sample may not be isotropic and that its absorption depends on the linear polarization state of the light. In the isotropic case, where $I_p=I_s$, the intensity I_D becomes constant as the modulated term becomes zero. In order to demonstrate the time dependence of I_D , the $\cos \phi$ -term can be expanded with the help of Bessel functions J_n , in this case known as Jacobi-Anger expansion given by:

$$\cos[\phi_0 \sin(\omega_m t)] = J_0(\phi_0) + 2 \sum_{k=1}^{\infty} J_{2k}(\phi_0) \cos(2k\omega_m t) \quad (3.29)$$

where the periodic phase difference ϕ given by equation 2.22 is already inserted. As the peak retardation ϕ_0 is actually a function of the wavenumber ν , also the Bessel functions depend on the wavenumber. Summation up till the second harmonic neglecting higher terms and inserting in equation 3.28 yields:

$$\begin{aligned} I_D(\nu, t) &= \underbrace{\frac{I_p(\nu) + I_s(\nu)}{2} + \frac{I_p(\nu) - I_s(\nu)}{2} J_0(\nu)}_{\text{dc}} + \underbrace{(I_p(\nu) - I_s(\nu)) J_2(\nu)}_{\text{ac}} \cos(2\omega_m t) \\ &= I_{\text{dc}}(\nu) + I_{\text{ac}}(\nu) \cos(2\omega_m t) \end{aligned} \quad (3.30)$$

for the first time derived by Hipps and Crosby [16]. The detected signal consists of a dc-term and an ac-term modulated at twice the frequency of the PEM. Considering the modulation of the interferometer, given by equation 2.5, the signal takes the form:

$$I_D(\delta, t) = \int_{-\infty}^{+\infty} [I_{\text{dc}}(\nu) + I_{\text{ac}}(\nu) \cos(2\omega_m t)] \cos(2\pi\nu\delta) d\nu \quad (3.31)$$

dependent on the periodic phase difference δ produced by the interferometer. Thus the detected signal is an interferogram actually consisting of the sum of two interferograms, one only modulated by the interferometer, and the other one additionally modulated by the PEM. They can be separated by means of a lock-in amplifier or digital signal processing, and in order to obtain the spectra I_{dc} and I_{ac} the two interferograms are Fourier transformed and yield:

$$\begin{aligned} I_{\text{dc}}(\nu) &= \frac{I_p(\nu) + I_s(\nu)}{2} + \frac{I_p(\nu) - I_s(\nu)}{2} J_0(\nu) \\ I_{\text{ac}}(\nu) &= (I_p(\nu) - I_s(\nu)) J_2(\nu) \end{aligned} \quad (3.32)$$

The important quantities are I_p and I_s by whose means the absorbances A_p and A_s can easily be calculated. They can be obtained by solving the equations 3.32

for I_p and I_s and assuming empirical correction factors g and G (defined below), which gives:

$$\begin{aligned} I_p(\nu) &= I_{dc}(\nu) - \left(\frac{G J_0(g \cdot \nu) - 1}{2J_2(g \cdot \nu)} \right) I_{ac}(\nu) \\ I_s(\nu) &= I_{dc}(\nu) - \left(\frac{G J_0(g \cdot \nu) + 1}{2J_2(g \cdot \nu)} \right) I_{ac}(\nu) \end{aligned} \quad (3.33)$$

On the one hand the constant factor G takes care of the different amplification and filtering of I_{dc} and I_{ac} and on the other hand the factor g takes care of the wavenumber dependence of the PEM. As mentioned in section 2.3.2 the change in the average of the detected intensity, actually representing I_{dc} , with respect to the wavenumber is very different in the two orthogonal directions. The same holds for the amplitude of the intensity modulation, actually representing I_{ac} , see figure 2.9. The influence of these effects on the spectra can be reduced through a calibration procedure, which delivers the factors G and g , see section 3.1.3.

Finally the absorbances are given by:

$$\begin{aligned} A_p &= -\log \left(\frac{I_p}{I_{p0}} \right) \\ A_s &= -\log \left(\frac{I_s}{I_{s0}} \right) \end{aligned} \quad (3.34)$$

where I_{p0} and I_{s0} are the background spectra indicating measurements without a sample which should theoretically be equal. As a matter of fact that cannot be achieved, because of possible inhomogeneities and the efficiency of the polarizer, which for wiregrid polarizers is about 99% in the infrared region. Thus the I_{ac} -term in equation 3.33 can never vanish and the normalization in equation 3.34 makes sure that this influence is small.

3.1.2 Phase-modulated Spectroscopic Ellipsometry

Ellipsometry is an efficient method to determine the optical properties of materials and mainly of surfaces. It is based on the measurement of the change of the polarization state evoked by a sample through light reflection or transmission. Ellipsometry is non destructive and highly sensitive. It allows to measure a spatial range from fractions of single layers up to micrometers and to control processes in real time. Spectroscopic ellipsometry employs broadband light sources, thus the complex refractive index or the dielectric function tensor in the corresponding spectral region can be obtained, which gives access to a large number of fundamental physical properties.

The result of an ellipsometry measurement is presented by the parameters ψ and Δ , that express the amplitude ratio and phase difference between p- and s-polarized light. By these two parameters the complex refractive index can be determined by applying the Fresnel equations, which define the amplitude transmission and reflection coefficients. From the ratio of these coefficients the ellipsometric parameters are derived and for transmission experiments they can be

expressed as:

$$\tan \psi \exp(i\Delta) = \frac{t_p}{t_s} \quad (3.35)$$

where t_p and t_s are the transmission coefficients given by the ratio of the amplitudes of the transmitted to the incoming light wave for p- and s-polarization respectively. Figure 3.11 shows a representation of an elliptical polarization state with the amplitudes of the polarization components in x- and y-direction denoted as E_{x0} and E_{y0} and can be represented by ψ as:

$$E_{x0} = \sin \psi E' \quad E_{y0} = \cos \psi E' \quad (3.36)$$

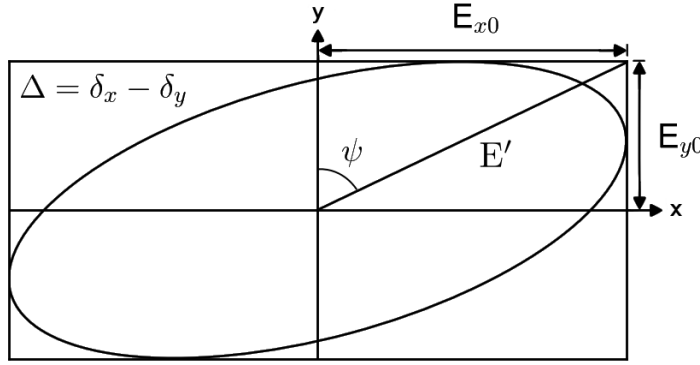


FIGURE 3.11: Representation of the elliptical polarization state by (ψ, Δ) -coordinates.

Therefore ψ represents the angle determined by the amplitude ratio between the polarization components. The phase difference Δ is given by $\Delta = \delta_x - \delta_y$. Thus the Jones vector can be formulated by the ellipsometric parameters as:

$$\begin{bmatrix} E_x \\ E_y \end{bmatrix} = \begin{bmatrix} E_{x0} \exp(i\Delta) \\ E_{y0} \end{bmatrix} = \begin{bmatrix} \sin \psi \exp(i\Delta) \\ \cos \psi \end{bmatrix} E' = \cos \psi \begin{bmatrix} \tan \psi \exp(i\Delta) \\ 1 \end{bmatrix} E' \quad (3.37)$$

The configuration of phase-modulated spectroscopic ellipsometry (PMSE) is similar to that of PMIRLD except that an analyzer is placed in front of the detector rotated at the same azimuth angle as the modulator, see reference [17]:

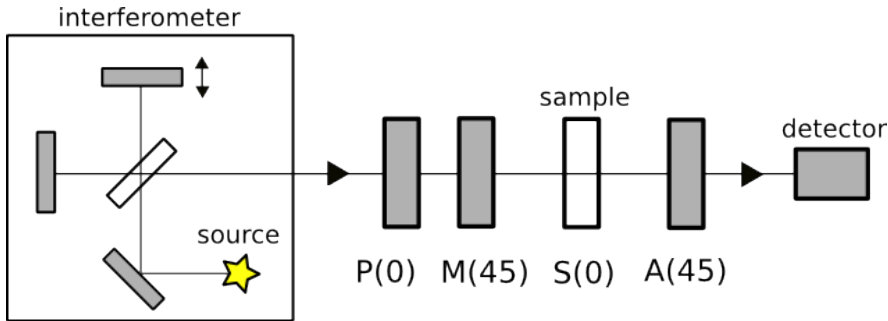


FIGURE 3.12: The optical configuration of PMSE.

The Jones matrices representing this setup are given by:

$$\mathbf{E}_{\text{out}} = \underbrace{\text{R}(-45) \begin{bmatrix} 1 & 0 \\ 0 & 0 \end{bmatrix}}_{\text{A}(45)} \underbrace{\text{R}(45) \begin{bmatrix} \sin \psi \exp(i\Delta) & 0 \\ 0 & \cos \psi \end{bmatrix}}_{\text{S}(0)} \cdot \underbrace{\text{R}(-45) \begin{bmatrix} 1 & 0 \\ 0 & \exp(i\phi) \end{bmatrix}}_{\text{M}(45)} \underbrace{\text{R}(45) \begin{bmatrix} 1 & 0 \\ 0 & 0 \end{bmatrix}}_{\text{P}(0)} \mathbf{E}_{\text{in}} \quad (3.38)$$

Considering the role of the interferometer in the alignment of the optical elements the influence of the partial polarization of the interferometer is kept minimal, when the polarizer is rotated to the direction, where the intensity has its maximum. Calculating the intensity yields following equation:

$$I(\phi) = I' [1 - \sin \Delta \sin(2\psi) \sin \phi - \cos(2\psi) \cos \phi] \quad (3.39)$$

where I' again accounts for constant factors like the incoming intensity. Including the analyzer results in an additional $(\sin \phi)$ -term, which can be expanded with the help of odd Bessel functions:

$$\sin[\phi_0 \sin(\omega_m t)] = 2 \sum_{k=1}^{\infty} J_{2k-1}(\phi_0) \sin[(2k-1)\omega_m t] \quad (3.40)$$

Inserting now equation 3.29 and 3.40 in 3.39 and neglecting terms involving higher frequencies gives the intensity the following form:

$$I(\nu) = I' \left[\underbrace{1 - J_0(\nu) \cos 2\psi}_{S_0} - \underbrace{2J_1(\nu) \sin \Delta \sin 2\psi}_{S_\omega} \sin(\omega_m t) - \underbrace{2J_2(\nu) \cos 2\psi}_{S_{2\omega}} \cos(2\omega_m t) \right] \quad (3.41)$$

In this equation a fundamental ω -term arises in addition to the dc and the 2ω components. The influence of the sample on the detected signal can be estimated as e.g. the ω -term will vanish, if no additional phase shift Δ is applied. It can also be noticed that the intensity would not be modulated, if there were no sample, resulting in $\Delta = 0$ and $\psi = 45^\circ$. As already seen in section 3.1.1 the modulation of the interferometer has to be considered and in this case yields the following interferogram:

$$I(\delta, t) = \int_{-\infty}^{+\infty} I'(\nu) [S_0(\nu) + S_\omega(\nu) \sin(\omega_m t) + S_{2\omega}(\nu) \cos(2\omega_m t)] \cos(2\pi\nu\delta) d\nu \quad (3.42)$$

which now is actually a sum of three individual interferograms. In order to obtain the three spectra S_0 , S_ω and $S_{2\omega}$ the interferograms have to be separated and Fourier transformed. By means of these spectra two ratios, R_ω and $R_{2\omega}$, are

defined [18]:

$$R_\omega = \frac{S_\omega(\nu)}{S_0(\nu)} = \frac{-2J_1(\nu) \sin \Delta \sin 2\psi}{1 - J_0(\nu) \cos 2\psi} \quad (3.43)$$

$$R_{2\omega} = \frac{S_{2\omega}(\nu)}{S_0(\nu)} = \frac{-2J_2(\nu) \cos 2\psi}{1 - J_0(\nu) \cos 2\psi} \quad (3.44)$$

from which the ellipsometric parameters ψ and Δ can easily be obtained. They take the following form:

$$\psi = \frac{1}{2} \cos^{-1} \left(\frac{R_{2\omega}}{J_0(\nu) R_{2\omega} - 2J_2(\nu)} \right) \quad (3.45)$$

$$\Delta = -\sin^{-1} \left(\frac{R_\omega [1 - J_0(\nu) \cos 2\psi]}{2J_1(\nu) \sin 2\psi} \right) \quad (3.46)$$

The ellipsometric measurements can be presented in the form of (ψ, Δ) -coordinates, which characterize the polarization state, or, in order to directly characterize the material, by using the complex optical density [19], given by:

$$D = \log \left(\frac{\tan \psi_b}{\tan \psi} \right) - i(\Delta - \Delta_b) \quad (3.47)$$

where the index b refers to a background measurement without a sample. The real part of D represents the relative amplitude attenuation, whereas the imaginary part describes the relative phase retardation caused by the material. Thus D refers to both, the dichroism and the birefringence of the sample. The same wavenumber-dependence of the modulation amplitude ϕ_0 of the PEM takes place in PMSE measurements, thus the same calibration procedure is applied, see next section 3.1.3.

3.1.3 Calibration Procedure

In order to remove the undesired influence of the wavelength dependence of the PEM, which results in spectral artefacts or in a slowly varying background, also known as Bessel background, various methods can be used [20].

In this thesis the calibration procedure is similar to that found in reference [21] and requires two independently obtained calibration spectra, from which new calibrated Bessel functions with the fitparameters G and g , see equation 3.33, are derived. The optical configuration is equivalent to the configuration of the intensity modulation in figure 2.8, but only the polarization component parallel to the incident light is measured. Thus the analyzer is set at the same azimuth angle as the polarizer and the configuration looks like this:

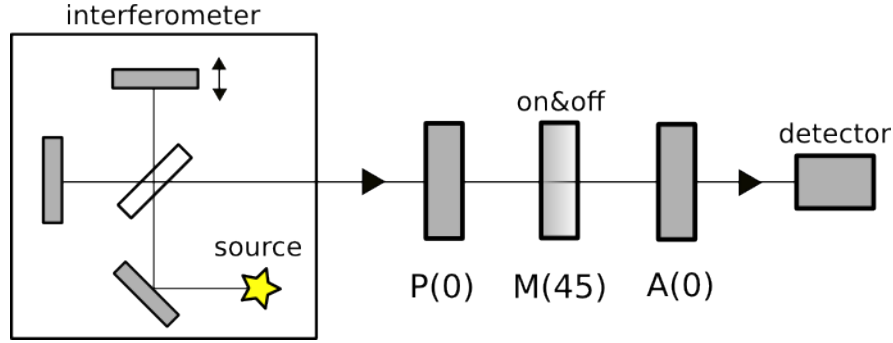


FIGURE 3.13: The optical configuration of the calibration procedure.

The first calibration spectrum is acquired, while the PEM is turned off, thus the incident light is not modified and the detected signal represents I' from equation 2.25. The second calibration spectrum is acquired, while the PEM is turned on, resulting in:

$$I_D(\nu, t) = I' \left[\frac{1}{2}(1 + J_0(\nu)) + J_2(\nu) \cos(2\omega_m t) \right] \quad (3.48)$$

From this signal two spectra are extracted:

$$I_{dc}(\nu) = \frac{I'}{2}(1 + J_0(\nu)) \quad (3.49)$$

and

$$I_{ac}(\nu) = I' J_2(\nu) \quad (3.50)$$

which are then divided by the first calibration spectrum I' and rearranged to lead to the following measured quantities, which shall theoretically correspond to the Bessel functions:

$$\tilde{J}_0(\nu) = 2 \frac{I_{dc}(\nu)}{I'} - 1 = G \cdot J_0(g \cdot \nu) \quad (3.51)$$

$$\tilde{J}_2(\nu) = \frac{I_{ac}(\nu)}{I'} = G \cdot J_2(g \cdot \nu) \quad (3.52)$$

In figure 3.14 the theoretical Bessel functions are fitted to the measured Bessel functions yielding the two fitparameters G and g , see equation 3.33.

The described calibration procedure has to be carried out before each series of measurement, because the polarizing effects of the FTIR spectrometer, mainly of the beamsplitter, described in section 3.3, producing partially polarized light, are sensitive to environmental influences and of course to adjustments of the spectrometer. A change of the aperture or the resolution also changes the beam characteristics such as the intensity, the collimation, the phase and the partial polarization. These effects depend on each other and influence the polarization properties. Further, the polarization efficiency of the wiregrid polarizers is wavenumber dependent. Thus the varying percentage, minimal one percent, of the perpendicular polarization component depends on many factors, which alter the incident polarization state and furthermore the influence of the PEM. Thus the calibration procedure accounts for these effects, too.

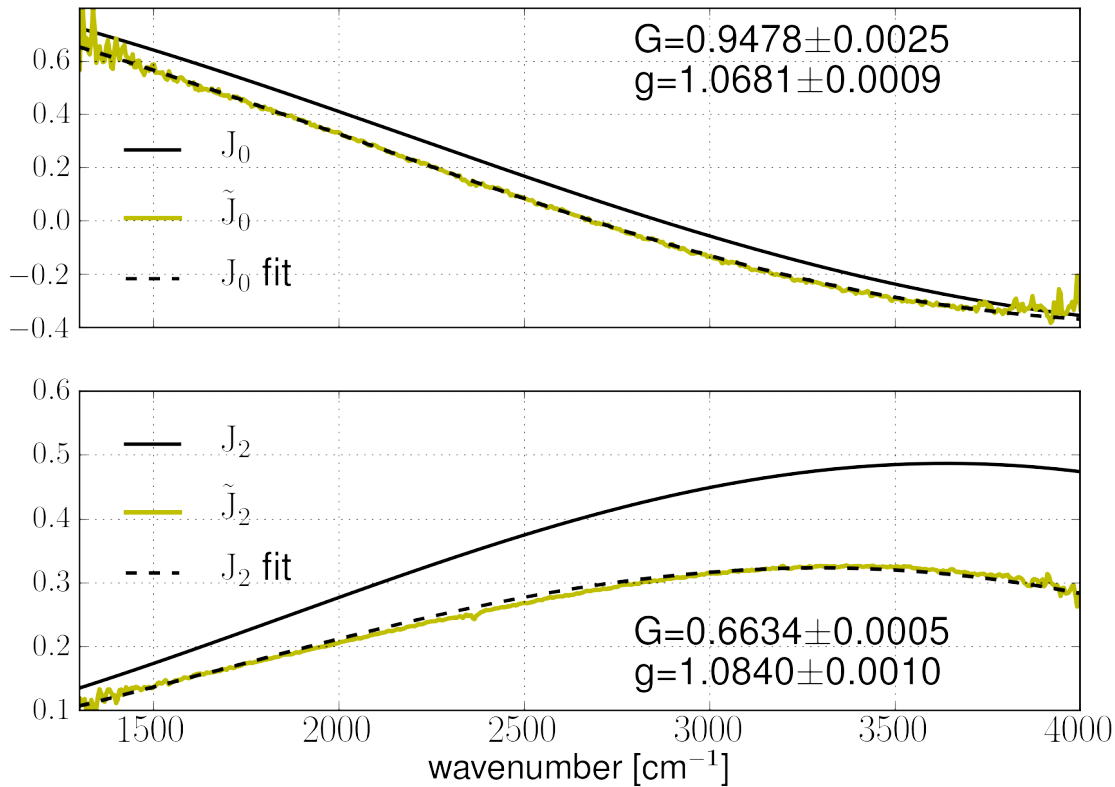


FIGURE 3.14: At the top the zero order and at the bottom the second order Bessel functions (theoretically, measured and fitted) are presented, with the corresponding fit parameters for a specific measurement.

3.2 Experimental Data Processing

The methods described above demand the simultaneous recording of two or three components dc, 1f and 2f of the signal at each mirror position. In PMSE these components produce the interferogram I_{dc} not modulated by the PEM and the modulated interferograms I_{1f} at the fundamental frequency and I_{2f} at doubled frequency of the modulator. In order to extract these frequency components from the detected signal a set of electronic filters and two lock-in amplifiers are necessary. Furthermore the continuous modulation by the interferometer overlays the PEM modulation and so the velocity of the moving mirror has to be reduced. The ideal situation is realized by successively stopping the mobile mirror during the measurement of one sampling point, which becomes possible by means of step-scan mode.

By this method, utilized in this work, the operator has the control over the single steps of the interferometer and thus over the time dependence of the measurement. Therefore the fast operating lock-in amplifiers become dispensable and digital

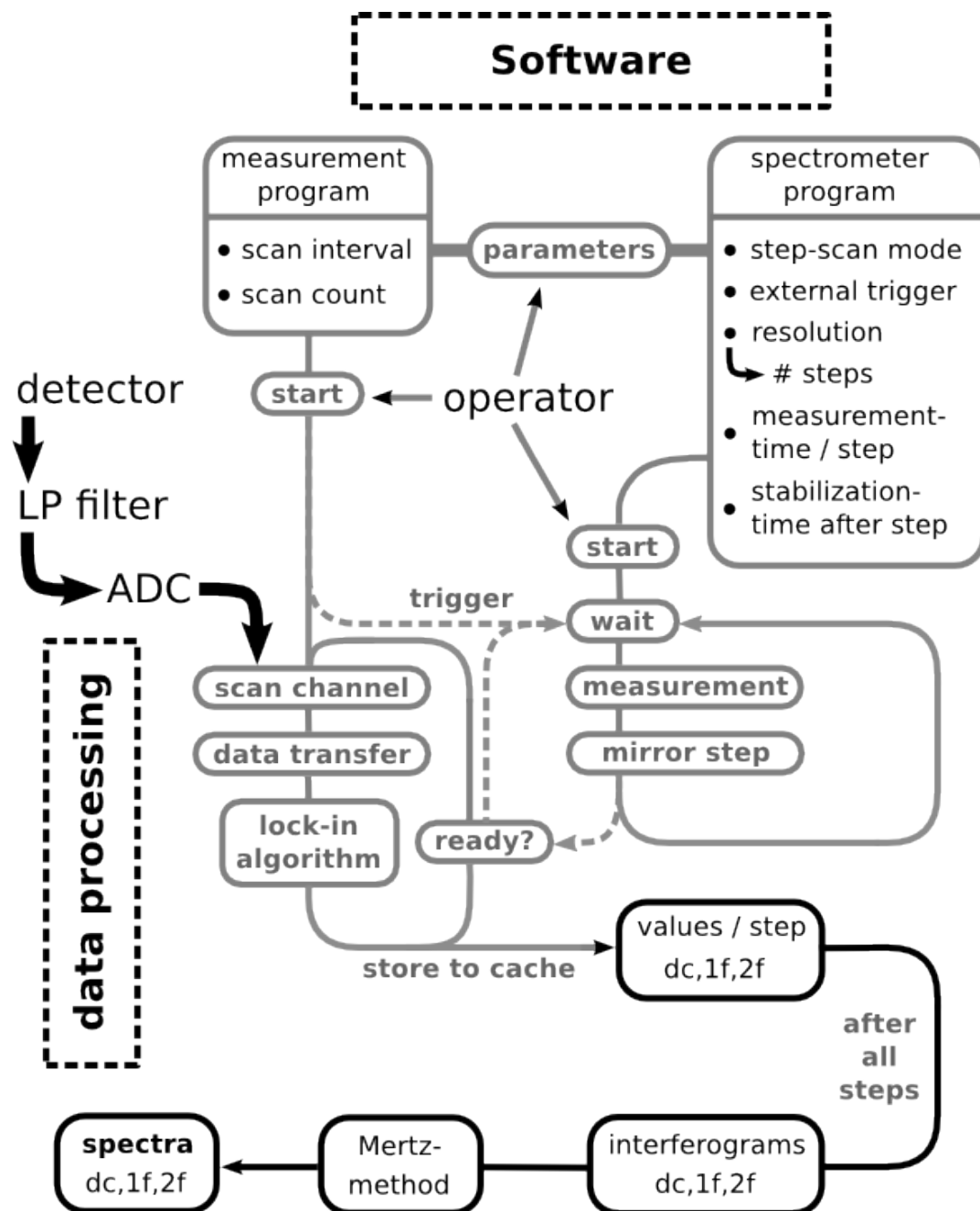
signal processing takes care of the PEM modulation. At each step the electrical signal provided by the MCT detector is low-pass filtered and transmitted to the 16-bit ADC. The Nyquist criterion [22] is by far fulfilled and the signal is oversampled with the maximal samplingrate f_s of the DAQ card (10 MHz).

Furthermore, at each step the signal is measured over a certain time and afterwards demodulated by means of a lock-in algorithm, which delivers the individual frequency components. The measurement time t per step has also an essential influence on the SNR which increases proportionally to \sqrt{t} , see equation 2.10. The SNR is inversely proportional to the bandwidth of the signal, therefore the ADC is preceded by an analog low-pass (LP) filter with a cut-off frequency of 100kHz. The lock-in algorithm is realized by Fourier transform of the signal, cutting out the specific frequency band and building the sum over all frequency components in this band representing the interferogram point at a determined mirror position. The obtained interferograms are then modified by zerofilling and by a possibly necessary baseline correction. Then the Mertz Method deals with the apodization and phase correction, and Fourier transformation delivers the desired spectra. The further treatment of the spectra to obtain the significant values according to the methods is processed afterwards.

It is important to notice that this measurement method of the spectra, taking several minutes, is time-consuming what is influenced by many factors. Firstly the use of step-scan mode slows down the measurement, but the same do factors such as the resolution, the speed of the lock-in algorithm or the stabilization time after each step to prevent mirror oscillations. Furthermore it is always a tradeoff between high SNR, high resolution and short measurement time. Thus this method is by far not suitable for real-time measurements of dynamic processes. There are many PMIRLD- and PMSE-studies carried out by means of different signal processing with lock-in amplifiers and in rapid-scan mode⁹ allowing real-time measurements.

The data processing method described above is depicted in the following flow diagram, where both the signal processing and the interplay of the two programs used, a measurement program controlling the entire measurement process and a program controlling the spectrometer, can be seen. The factors scan interval and scan count determine the samplingrate and measurement time. The program controlling the spectrometer is synchronized with the measurement program by sending triggers.

⁹Rapid-scan indicates that the mirror moves continuously.



3.3 Instrumentation

The beamsplitter: Germanium-layer on Potassiumbromid-substrate

As already mentioned, the efficiency of the beamsplitter affects the quality of FTIR spectroscopy measurements, especially of polarization experiments, because the efficiency is different in the two polarization directions. In figure 3.15 the operation principle of a sandwich beamsplitter is depicted. Ideally the substrate should be highly transmitting and suppress surface reflections. The reflectance and transmittance of the layer should be equal to 0,5 across the entire spectrum optimized for an incidence angle of 45° . So the efficiency given by $\eta(\nu) = 4R_\nu T_\nu$ would become unity.

In order to illustrate the difficulty in achieving high efficiency, the reflectance R of Germanium with an assumed refractive index $n \approx 4$ at 45° incidence can be calculated by means of the Fresnel equations, which give $R_p = 0,24$ and $R_s = 0,49$ delivering efficiencies $\eta_p = 0,73$ and $\eta_s \approx 1,0$. Thus, even though Germanium is a good material for s-polarized radiation, its efficiency for p-polarized radiation is low [6]. This is why beamsplitters polarize the beam in interferometers.

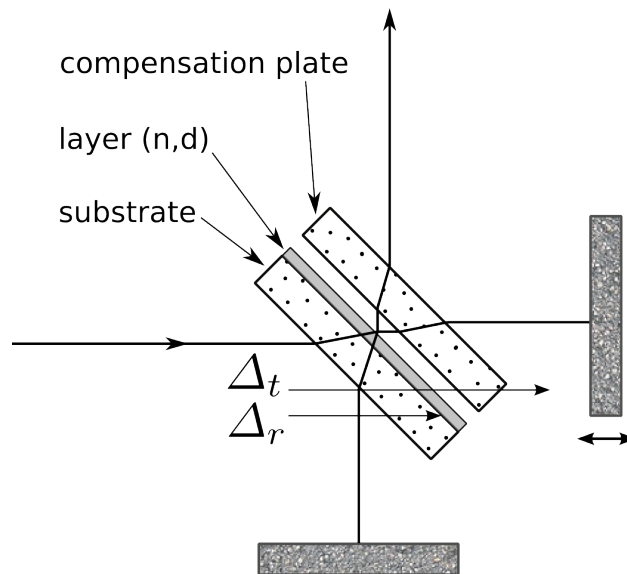


FIGURE 3.15: Schematic representation of the beamsplitter.

Furthermore the refractive index of the substrate should be constant across the entire spectral range if all wavelengths are to be in phase at the same point. Δ_t and Δ_r in figure 3.15 indicate that the reflected beam is passing the substrate more often than the transmitted beam what leads to a different phase shift. In order to avoid the effect of dispersion the splitted beams have to pass the dispersive substrate equally often, therefore a compensation plate of exactly the same thickness and material as the substrate is mounted in the optical path or combined with the beamsplitter indicating a sandwich beamsplitter. KBr restricts the spectral region

from approximately 400 cm^{-1} to approximately 7000 cm^{-1} , where its refractive index and consequently its transmittance are quite constant, see figure 3.16.

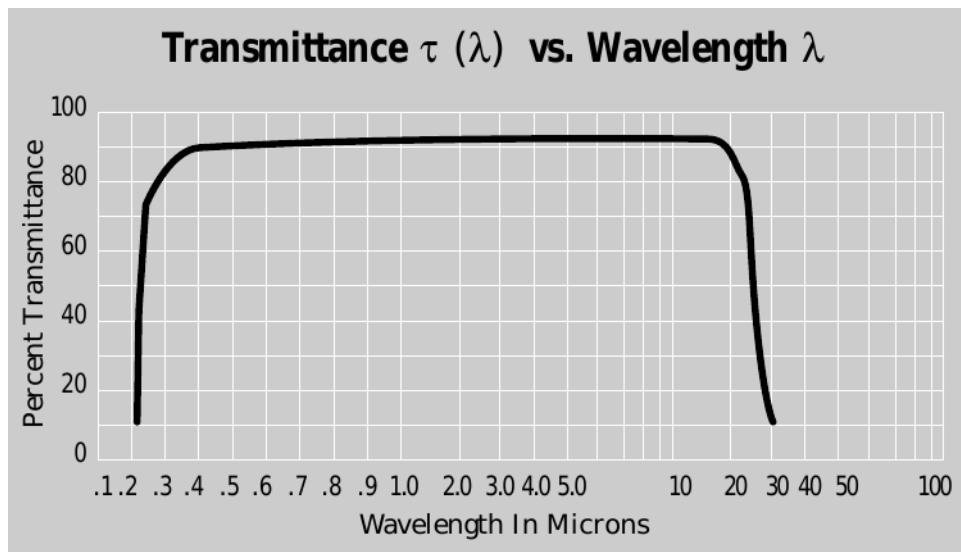


FIGURE 3.16: Transmittance of KBr. Image taken from a datasheet of ISP optics.

The layer can generate interference fringes by multiple internal reflections, therefore the thickness d has to be selected in such a way that the first fringe already covers the spectral range of interest. By means of multiple layers the spectral region can be increased by sacrificing efficiency at the same time.

The FTIR spectrometer: Bruker Vertex 70 [23]

This spectrometer already includes the MIR-lightsource, a nichrome wire, which is heated to about 1100 K . Through an adjustable aperture the light is guided to the Michelson interferometer consisting of two movable mirrors¹⁰ and the already mentioned beamsplitter. After the interferometer a mirror mounted on a stage can guide the beam outside the spectrometer. The position of this mirror can undesirably alter after the stage was moved, because the stage does not stop at exactly the same place again. This causes a further, mainly directional change of the output beam.

The Bruker spectrometer can operate in step-scan mode, which offers the ability to time-resolved spectroscopy. In this mode the movable mirror is held at equally spaced points for fixed short periods and steps rapidly between these points. If a reproducible time-dependent process is executed during each step, time dependent spectra are obtained, which can characterize the dynamic process. It is possible to trigger the single steps, which is done in this work.

¹⁰In this spectrometer two mirrors are constructionally connected and move together like a seesaw. This has the advantage of being more stable concerning thermal expansions.

The photoelastic modulator: Hinds PEM-90 Series II/ZS 37 [24]

This PEM is used to generate broadband polarization modulation in the mid-infrared electromagnetic region. The optical element consists of a zinc selenide (ZnSe) crystal of octagonal shape, which is stimulated by two piezoelectric transducers to the fundamental oscillation at a fixed frequency of 37 kHz. The symmetric PEM changes the refractive indices n_x and n_y at the same time, but with opposite signs, see figure 3.17. Thus this modulator provides a symmetric retardation distribution, a high range of retardation modulation and a large optical aperture. At half-wave peak retardation the wavenumber-limitation of the PEM reaches 1000 cm^{-1} . The other side of the available spectral region is solely limited by the transmission limit of ZnSe and is approximately 20000 cm^{-1} .

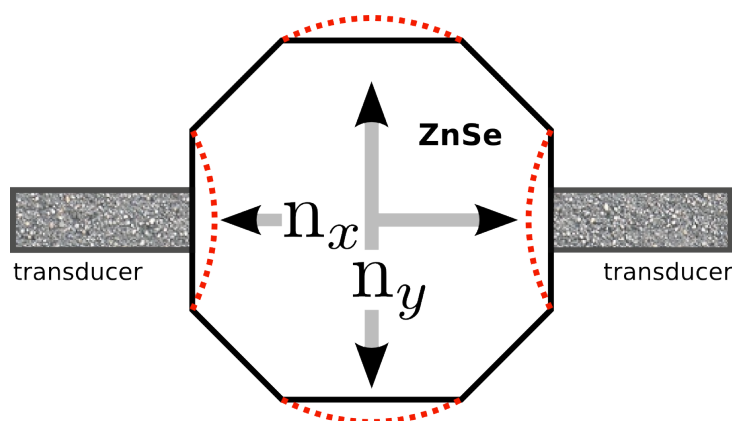


FIGURE 3.17: Schematic representation of the octagonal PEM and its oscillation (red).

The MCT-detector: Vigo System PVMI-3TE-8 [25]

In FTIR spectroscopy the detector is, besides the beamsplitter, the main factor limiting the width of the spectrum. This thermoelectrically cooled detector contains a photodiode consisting of an alloy of mercury-cadmium-telluride (MCT). In this semiconductor an infrared photon is detected, when its energy is sufficient to kick an electron from the valence band to the conduction band. Thus cooling the detector is important to reduce noise due to thermally excited charge carriers. The size of the bandgap determines the wavenumber-limitations. According to the datasheet this detector is optimized for operation at $\sim 8 \mu\text{m}$ and has a detectivity $D^* \geq 4 \cdot 10^9 \text{ cm}\sqrt{\text{Hz}}/\text{W}$ at this wavelength. D^* is defined as:

$$D^* = \frac{\sqrt{A}}{\text{NEP}}$$

where A is the area of the photosensitive region of the detector, here $A=1\text{mm}^2$, and NEP is the noise equivalent power, see equation 2.10.

The DAQ card: Adlink PXI-9816 [\[26\]](#)

This data-acquisition card is equipped with a 16-bit ADC and its analog input channel has a range of ± 1 V and a maximum sampling rate of 10 MS/s. The smallest detectable change in voltage is equal to $30,52 \mu\text{V}$ leading to the power of the system noise of $0,092 \text{ mV}_{rms}$.

4. Results

4.1 The Stretching Device

In order to directionally affect the optical properties of the sample and to have control over this influence a stretching device is used. By its means the film can be clamped in two vices and can be stretched in the direction, which is given by the vice mounted on a linear stage. Thus the stretching direction can be selected by mounting the film in the specific direction. The magnitude of the individual stretching steps is selected through a software controlling the stage. Furthermore a force sensor is attached to the moving vice, by whose means the tensile force can be measured allowing conclusions about the mechanical, respectively elastic properties of the sample. Young's modulus (or modulus of elasticity) E is given by the ratio of the stress σ to the axial strain ε , see reference [27]:

$$E = \frac{\sigma}{\varepsilon} = \frac{F/A_0}{\Delta L/L_0}$$

where F is the tensile force, A_0 the cross-sectional area, ΔL is the amount by which the length of the film changes and L_0 the length of the mounted film respectively the distance between the vices.

The film samples were cut out of a PLA bag. We have to distinguish between lengthwise and crosswise cut, see figure 4.18 at the right. Thus after mounting them on the stretching tool the force direction was either lengthwise or crosswise. In figure 4.18 Young's modulus of the film is shown and displays a distinct difference in elastic behavior between the lengthwise and crosswise directions. The lengthwise cut probe broke already at $\Delta L \approx 43$ mm, whereas the crosswise cut probe broke at $\Delta L \approx 110$ mm. Apparently the film had already been purposely stretched and oriented during the manufacturing process, because oriented polymer films give more tensile strength in the direction perpendicular to the orientation of the chains.

Equation 2.18 states that the induced phase difference between the polarization components is directly proportional to the applied stress, therefore this result can also be shown by means of polarized infrared spectroscopy, see section 4.4. The process of relaxation is neglected here and every measurement is executed after the film had enough time to relax, until no more change in the measured force is noticeable.

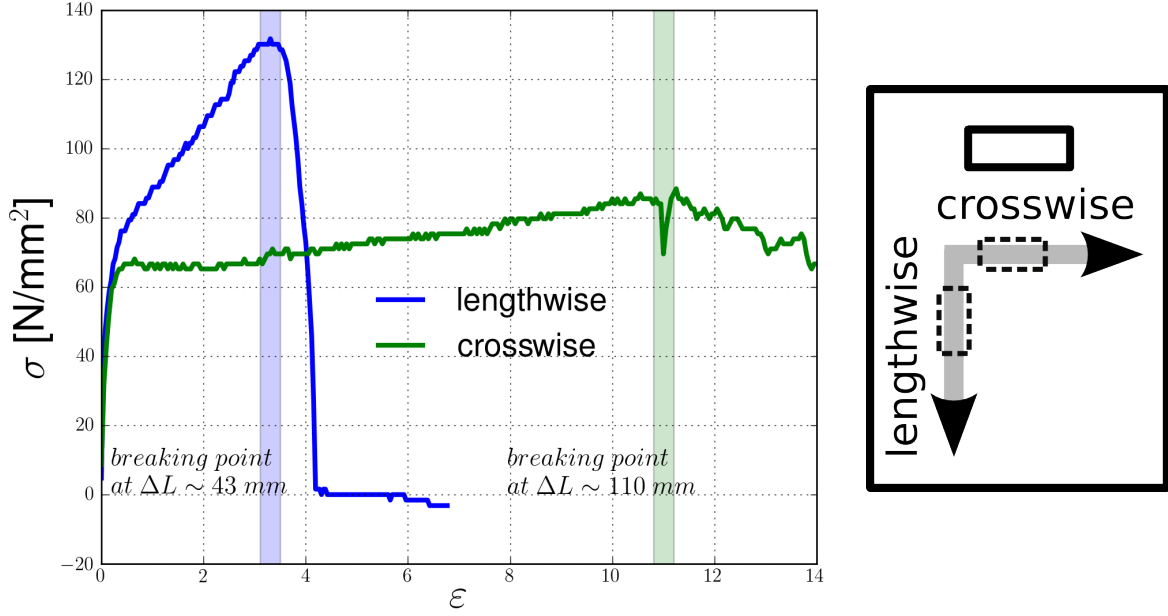


FIGURE 4.18: Young's modulus of the PLA film for the two different directions.

4.2 IRLD

4.2.1 Static IRLD

The dichroic difference is obtained from spectra, which are recorded sequentially with the infrared radiation polarized parallel and perpendicular to the uniaxial force direction of the stretching tool at normal incidence. In order to calculate the absorbances the static measurements require the recording of two background spectra without the sample, one for each polarization direction, since the beam-splitter is polarization-sensitive. Furthermore other components such as lenses, windows or the detector can show anisotropic behaviour affecting the state of polarization.

The measurement setup consists sequentially of the spectrometer, a rotatable polarizer, the stretching tool with the sample and a lens focusing the transmitted light on the detector. The signal is amplified and then digitized by the 24-bit ADC embedded in the spectrometer Bruker Vertex 70. The spectrometer software deals with the phase-correction and Fourier transformation. For each spectrum, 64 scans are averaged at a spectral resolution of 4 cm^{-1} . The stretching tool executes 4 mm steps each time recording two spectra corresponding to the orthogonal polarization components.

In figure 4.19 the resulting dichroic difference spectra at the different stretching steps are shown. At the top of this figure an absorbance spectrum is shown in order to illustrate the additional information obtained by the dichroic difference

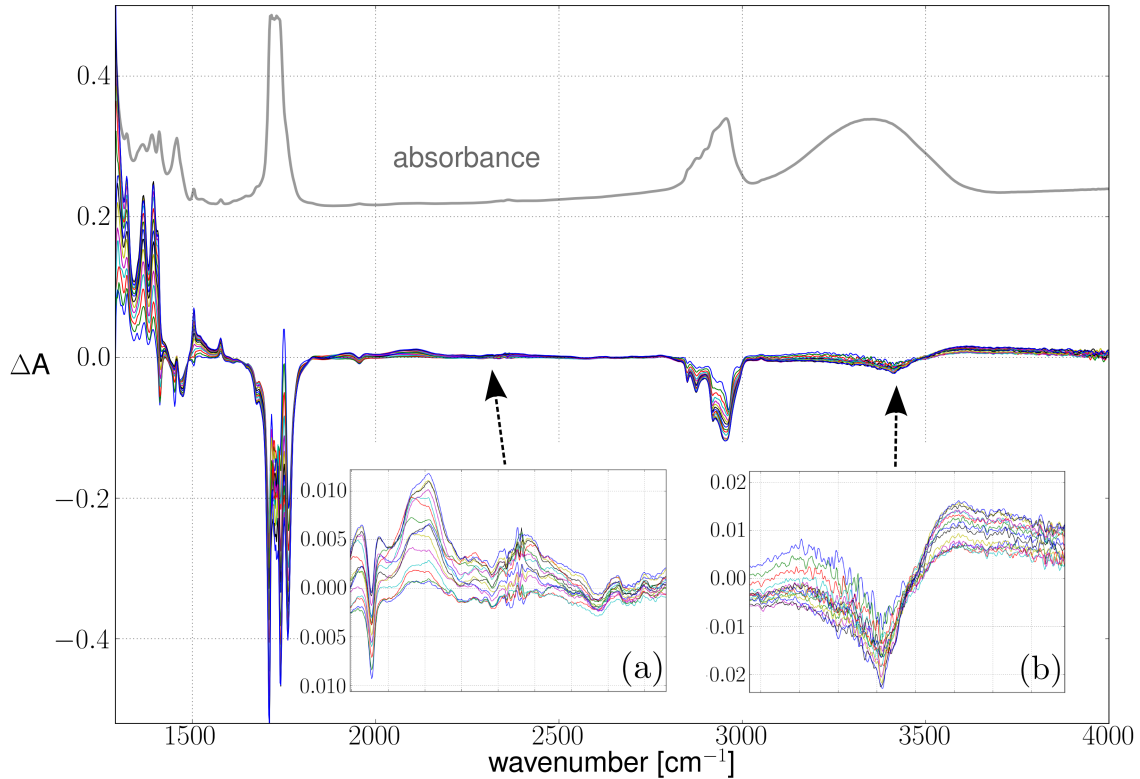


FIGURE 4.19: The dichroic difference of the PLA film for each stretching step (4 mm) till the breaking point at 66 mm. At the top the absorbance of the unstretched film is shown, scaled to fit in this plot. The two plots at the bottom illustrate baseline effects.

spectra which are defined as parallel minus perpendicular absorbances, see equation 2.21. So there appear positive bands indicating functional group transition dipoles aligning parallel to the stretching direction, respectively parallel to the polymer chain. On the other hand there are negative bands arising from transition dipoles perpendicular to the aligned chains. Furthermore it is important to notice that some spectral features vanish and others arise in the dichroic difference spectra. That is because some functional groups are isotropic and aren't accessible to orientation through mechanical stress, whereas specific vibrational modes evolve from orientation or show a shift in intensity and frequency unveiling distinct spectral features. The preorientation of the polymer sample, as already exhibited by means of Young's modulus of the film, can also be clearly revealed by the vibration-specific dichroic peaks already existing before the mechanical deformation (blue line with $\sigma = 0$ has the smallest peaks).

Another conspicuous feature is shown in the two insets of figure 4.19, which magnify the baseline around zero. As mentioned in section 2.2.3 baseline effects occur mainly because of wavenumber-dependent effects such as scattering and reflection. The spectral features at the baseline hardly change their shape during the stretching, but rather increase or decrease as the film becomes thinner. The dichroic difference of a given vibrational band arises not only from the polymer orientation but also from the relative dipole strength of the infrared absorption

and the sample thickness [28]. In 4.19(a) the bands, most likely evoked by nitro-plasticizers consisting of nitrogen compounds, have inherently low intensities and thus they easily become indistinct through baseline effects. That makes quantitative analysis difficult, because baseline variations give large experimental error. As shown in reference [29], it is possible to reduce the baseline effects by means of multiplicative factors or subtractions, which account for variations in sample thickness and minimize spectral differences. This correction procedure is not realized in this work, because enough sharp spectral features hardly influenced by baseline effects are recorded. It is also important to notice, that the CO₂-absorption from the air at approximately 2340 cm⁻¹ doesn't appear in the dichroic spectra, which indicates constant environmental influences.

In 4.19(b) a small feature evoked by hydrogen intermolecular bonds is shown, which, such as the plasticizers, hardly change by the applied stress. The broad O-H absorption band is missing in the dichroic difference spectra, because the hydrogen-bonded O-H groups are randomly aligned. This hydrogen-bonded morphology provides the distinctive elastomeric thermal and mechanical properties of the material. The hydrogen-bonded components being more viscous show negative dichroic response whereas the free components demonstrate an elastic positive response [30].

The specific dichroic peaks are listed and assigned to certain vibrational modes in table 4.3. Further, their orientation is assigned according to a negative or positive dichroic response. The two biggest negative bands arise from vibrations of the C-H stretching modes at 2850 - 2963 cm⁻¹ and the C=O functional group at 1710 - 1761 cm⁻¹. As can be seen in figure 2.2, these groups are aligned perpendicular to the backbone of the polymer and thus display negative difference bands.

Band (cm ⁻¹)	Assignment	Orientation
2963	(C-H) str.	⊥
2920	(C-H) str.	⊥
2874	(C-H) str.	⊥
2850	(C-H) str.	⊥
1761	(C=O) str.	⊥
1741	(C=O) str.	⊥
1710	(C=O) str.	⊥
1505	(C-N)+(N-H)	
1452	(C-H ₂) ben.	⊥
1412	phenyl ring	⊥
1394	(C-H ₂) wag.	
1366	(C-H ₂) wag.	
1320	(C-N)+(N-H)	
<1300	(C-O-C) str.	

TABLE 4.3: Assignment of the dichroic bands (str.=stretching, ben.=bending and wag.=wagging)

In figure 4.20 the C-H stretching band is shown in detail. The unstretched film already features negative dichroic peaks, which become more distinct or arise, as the peak at 2920 cm^{-1} , during the stretching. The emergence of this negative peak directly represents a change in direction of a C-H-bond. At this particular wavenumber, respectively energy, no distinct vibration could be excited before stretching. During the stretching process the chains become aligned in the stress-direction and thus the lateral groups extending from the backbone become aligned perpendicular to this direction causing the emergence of new absorption peaks.

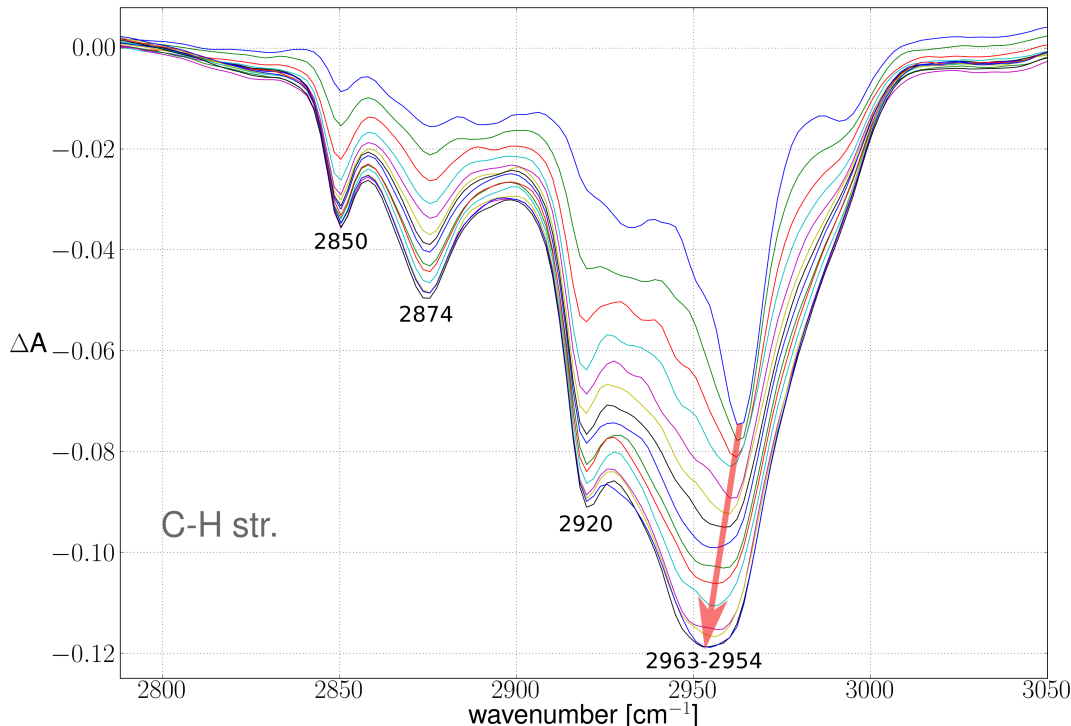


FIGURE 4.20: The dichroic difference of the C-H stretching mode. The arrow indicates the frequency shift and points towards increasing stress.

The peak at around 2963 cm^{-1} (at $\sigma=0$) performs not only a frequency shift to lower frequencies, but also becomes noticeably broader. The different absorption peaks clearly interact as the change of the bond angles or of the distance between atoms lead to a distortion of neighboring bonds that can slightly alter their vibrational normal modes. The two peaks at 2850 cm^{-1} and 2874 cm^{-1} indicate an increase in the dipole strength of the related vibration.

Regarding the carbonyl region, shown in figure 4.21, two peaks at 1710 cm^{-1} and 1761 cm^{-1} hardly change their shape as they are related to hydrogen-bonded components. Whereas the first one increases a little bit, the second even decreases. One interpretation is that the nitroplasticizer is disrupting hydrogen bonding in the hard segments, so that the bound component is decreasing [29]. A further peak at 1741 cm^{-1} arises through the stretching process and increases very fast indicating a free, unbound component. Furthermore almost all dichroic peaks show a very small frequency shift, which is explained by a temperature change in reference [31].

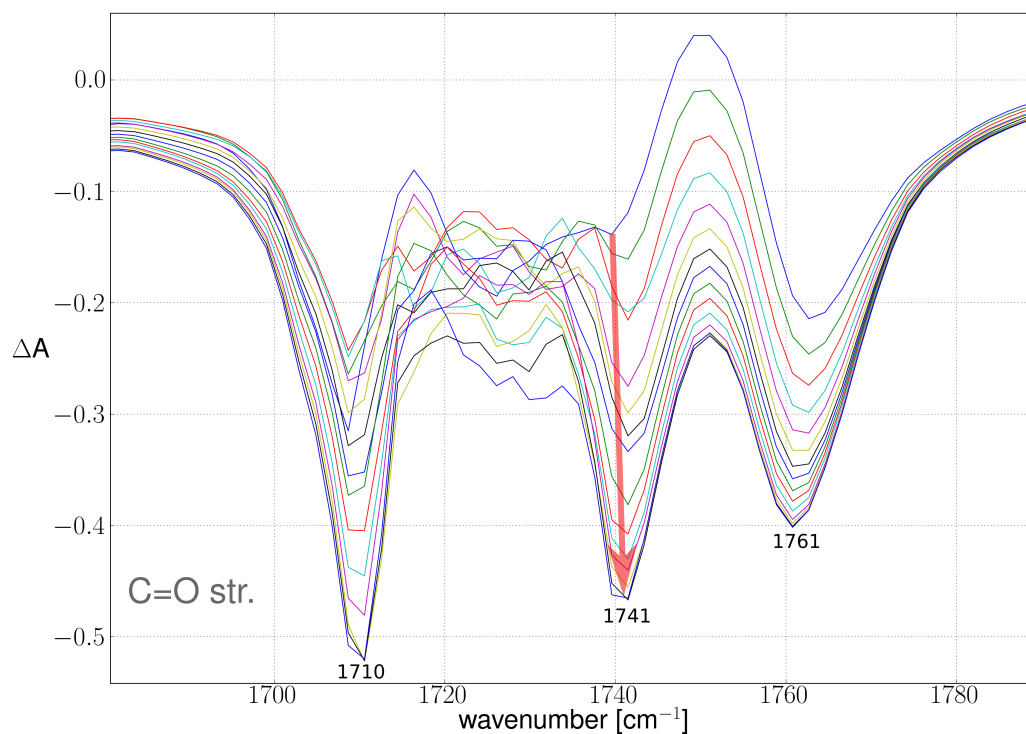


FIGURE 4.21: The dichroic difference of the C=O stretching mode. The red arrow points towards increasing stress.

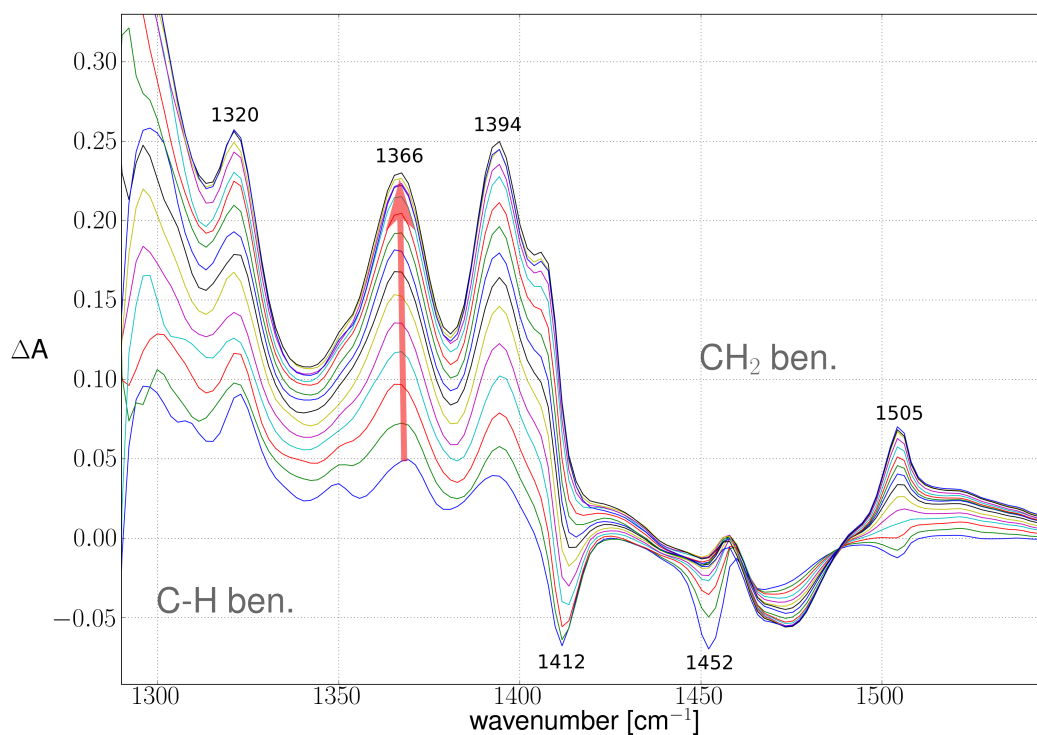


FIGURE 4.22: The dichroic difference of the C-H and CH_2 bending mode. The red arrow points towards increasing stress.

The remaining spectral region below 1550 cm^{-1} is complicated as there are significant contributions from both the hard and soft segments. Therefore the bending modes, which alter the bond angles between the different bonds, can show positive and negative dichroic peaks. At 1505 cm^{-1} a peak, belonging to a nitrogen compound likely from a plasticizer, actually shows both. Before stretching it is slightly negative and on the other hand the mechanical stress turns the peak upward.

The existing negative peak at 1452 cm^{-1} corresponding to the CH_2 -bending mode vanishes upon stretching. This indicates, that this component belonging to the soft segment possibly loses its hydrogen-bonds during stretching. Thus it becomes unbound and randomly oriented. The bands at 1366 and 1394 cm^{-1} are largely comprised of the wagging motion of CH_2 groups. In addition, the 1394 cm^{-1} band begins to overlap with the 1412 cm^{-1} band belonging to a phenyl ring, which shifts its frequency and changes its orientation from perpendicular to parallel to the chain-axis [30]. The dichroic band at 1320 cm^{-1} likely corresponding to a nitroplasticizer doesn't change its shape, indicating that these small molecules remain randomly oriented upon tensile deformation. Below 1300 cm^{-1} various C-O-C vibrational modes arise, but the the MCT-detector limits the spectral region and thus these modes can't be resolved.

The infrared linear dichroism spectra visualizes the two-phase microstructure of hard and soft domains in this PLA film. The hard segments, composed of polar materials, can form hydrogen bonds and thus tend to cluster or aggregate into ordered hard domains, whereas the soft segments form amorphous domains. The hydrogen-bonding interactions between the hard and soft domains are one of the key elements in determining stress-strain properties of polymers [30]. The PLA film responds to tensile deformation by uncoiling a portion of the soft segments supplying the elasticity, while the hard segments become aligned opposite to the stress direction and supply the strength.

4.2.2 Phase-modulated IRLD

By means of modulating the phase difference between the two polarization components the two orthogonal absorbances are obtained as described in section 3.1.1. The measurement setup consists sequentially of the spectrometer, a polarizer, the PEM, an aperture in order to narrow the beam diameter to approximately 2 mm, the stretching tool whereon the sample is clamped and a lense focusing on the detector. The signal is lowpass filtered ($f_g=100\text{ kHz}$) and then digitized by a 16-bit ADC. The exact signal processing is described above. The spectrum is recorded with a spectral resolution of 4 cm^{-1} in step-scan mode. Before each step the moved mirror has 8 ms in order to stabilize and the signal is then recorded for 1,6 ms. The stretching tool executes 2 mm steps after each measurement. A zero filling factor of 4 is used. Before a series of measurements the described calibration procedure has to be processed delivering the calibration parameters, see section 3.1.3. The experiment requires an exact adjustment of the angle (estimated error: $\pm 0.5^\circ$) between the polarizer and the modulator in order to minimize the already vanishing ω -term from the signal and to achieve the same modulation of each polarization component.

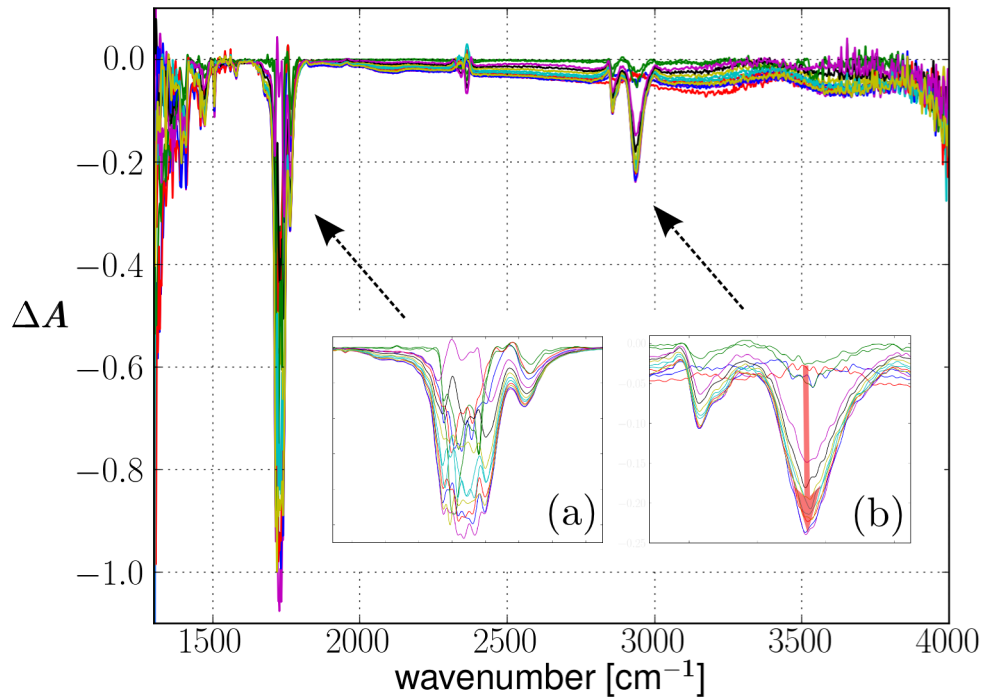


FIGURE 4.23: The dichroic difference spectra. The two main peaks are magnified in (a) and (b). The red arrow points towards increasing stress.

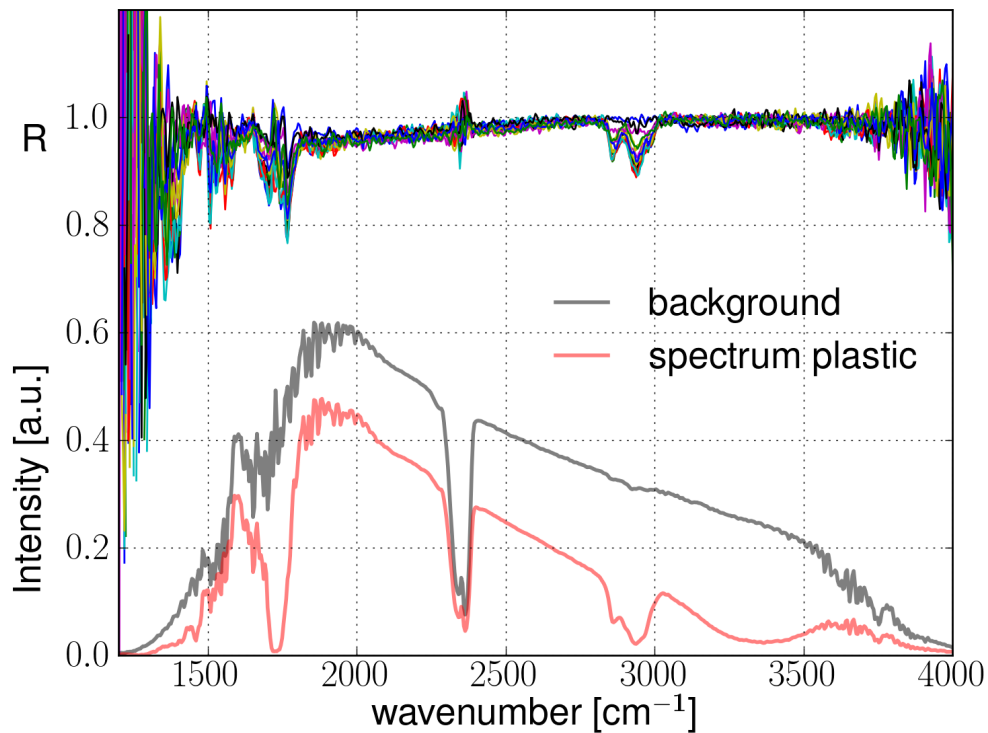


FIGURE 4.24: At the top the dichroic ratio spectra. At the bottom the background spectrum and one spectrum of the film.

In figure 4.23 the dichroic differences and in figure 4.24 the dichroic ratios obtained by PMIRLD are shown. The results clearly exhibit less peaks, different baseline effects and more noise as in the results of the static measurements. First of all it has to be mentioned that the samples were cut out from a new PLA bag, because the bag previously used was unfortunately lost. Thus the absence of some small peaks, which are resolved by the static measurements, doesn't necessarily mean that these peaks cannot be resolved by this method. It is also possible that the constitution of the new bag is somehow different. Furthermore, this sample was measured over and over during about 4 months, thus the degradation process, mainly hydrolysis, can have potential influence on the spectra. Hydrolysis implies losses in free and gains in hydrogen-bonded components. This is consistent with the fact, that almost all dichroic peaks are negative indicating the absence of the unbound components at wavenumbers smaller than 1600 cm^{-1} , which previously aligned parallel as measured by the static method.

A possible correction of the baselines, drifting apart with increasing wavenumbers, is neglected here, because the striking problem is the noise produced by measuring in step-scan mode, which will be discussed in section 4.5. The two big dichroic peaks can be resolved with the modulated method, but other smaller peaks aren't really significant. In addition the multiple pointed small peaks evoked from humidity of the ambient air, mainly at the two ends of the spectra, see figure 4.24 at the bottom, make the spectral analysis difficult and thus circumscribe the useful area of the spectra. So the anticipated improvement concerning environmental effects cannot be observed, as also the CO_2 -peak at 2340 cm^{-1} reveals some spectral features in the dichroic spectra. In figure 4.23(a) and (b) the two big peaks are magnified and show untrustworthy jagged shapes. All these erroneous spectral features originate primarily from recording the spectra in step-scan mode.

Quantitative treatments of molecular orientation often require knowledge of the dichroic ratio. However, in regions where the sample absorption is very weak, calculation of the dichroic ratio involves taking the ratio of noise on the baseline of A_p and A_s when both parameters are approximately zero. This is the reason why the dichroic ratio in figure 4.24 at the top is much more affected by noise than the dichroic difference spectra. Thus, if qualitative or semiquantitative information is all that is required, the dichroic difference spectrum is more useful than the dichroic ratio.

4.3 Phase-modulated Spectroscopic Ellipsometry

The optical configuration of PMSE differs from PMIRLD only in the second polarizer mounted in front of the detector. As shown in section 3.1.2 this results in an additional frequency-term in the signal delivering the information about the phase of the polarization components. Thus an additional adjustment of the angle of the analyzer is required (estimated error: $\pm 0.5^\circ$). The measurement parameters also remain the same as above. In figure 4.25 the amplitude angle ψ and in figure 4.26 the phase difference Δ obtained by PMSE are shown. The calculation of the optical density similar to the refractive index, see equation 3.47, brings no further

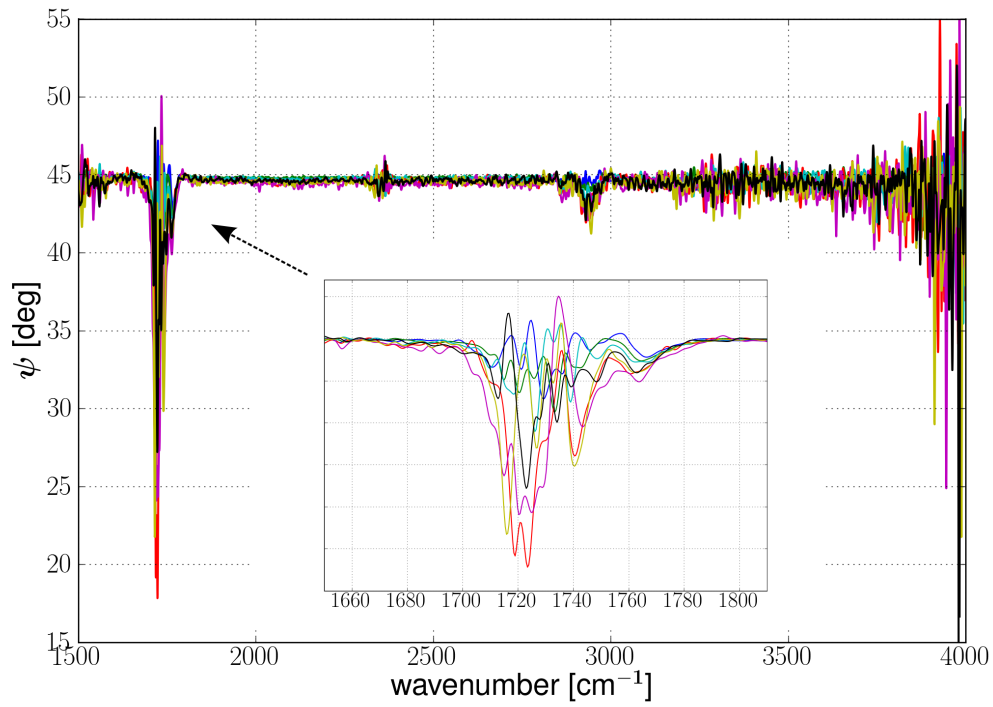


FIGURE 4.25: The amplitude angle ψ between the two polarization components.

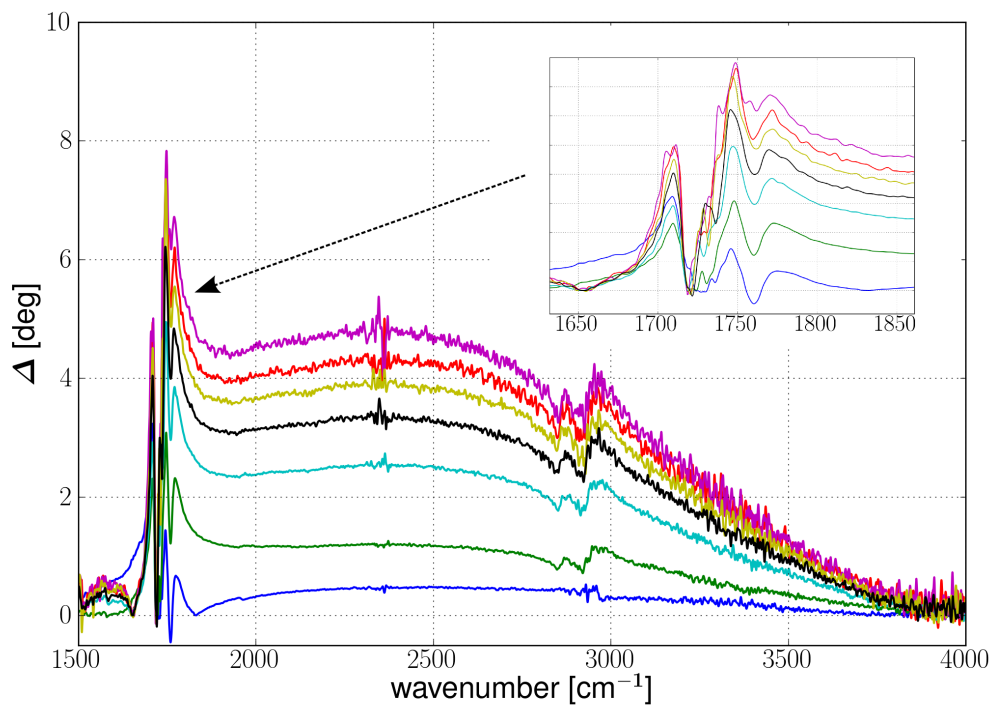


FIGURE 4.26: The phase angle Δ between the two polarization components.

insight as its characteristics do not differ from Δ and ψ .

The ψ -spectra representing the amplitude ratios between the polarization components can reveal the dichroic behavior of the film, but are also affected by the low SNR of step-scan measurements. Furthermore the amplitude angle ψ is comparable to the dichroic ratio and therefore implies more noise as in the dichroic difference spectra, as mentioned above. The second polarizer additionally attenuates the intensity leading to a smaller signal. The strong C=O-peak is almost similar to the peak measured by PMIRLD, whereas the C-H-peak at approximately 2900 cm^{-1} is comparatively small and nearly in the range of the CO₂-peak, which again is not canceled out. The Δ -spectra show the typical wavelength-dependent change of the phase in the area of absorptions. The phase retardation, given by $\Delta = \delta_2 - \delta_1 = \Delta n k_0 d$, is not only proportional to the phase difference of the two polarization components but also to the thickness of the film, which changes during the stretching process. Thus the actual change in phase difference with respect to the stretching steps should be more linear, if only the decreasing thickness of the film would be considered, which was not measured.

Spectroscopic ellipsometry opens the way to various interpretation schemes and enables the calculation of the optical constants over a broad spectral range. These further evaluations, including correction and fitting of the data, are out of the scope of this work. The increasing noise in the Δ -spectra is proportional to the intensity of the signal and will be discussed in section 4.5.

4.4 Configuration Between Crossed Polarizers

In order to evaluate the benefit of polarization dependent FTIR spectroscopy the stretching process is investigated for comparison by means of classical unpolarized FTIR spectroscopy and in crossed-polarizers configuration. In figure 4.27 the unpolarized absorbance spectra of the PLA film are shown. The spectra are recorded with a resolution of 4 cm^{-1} until the film broke at an elongation of approximately 10 cm. As the thickness of the film decreases during the stretching process more and more light is transmitted leading to a decrease of the absorbance spectra. This decrease is quite small and apparently proportional to the intensity. As already mentioned in section 3.3 the beam from the FTIR spectrometer is not unpolarized but rather polarized up to ~ 15 percent dependent on the wavenumber. Thus also in the classical absorbance spectra polarization-dependent effects can appear. These effects have no significant influence in the recorded spectra and are neglected here. The stretching process and structural changes of the material can not be observed by means of classical infrared spectroscopy.

The crossed-polarizers configuration implies that theoretically no light can pass to the detector. Because actually the polarizers let pass approximately one percent of the light, in the crossed-polarizers configuration a very small noisy spectrum can be recorded. This spectrum is not suitable for the calculation of the absorbance, thus figure 4.28 shows the transmittance spectra of the stretching process. Even the unstretched film causes a significant change in polarization mainly due to the change of the phase by transmission. Near the breakpoint of the film the eightfold

transmittance in comparison to the unstretched state is achieved. So the crossed-polarizers configuration shows a high sensitivity, because the smallest change in the state of polarization is detectable. But it is not possible to characterize this change further and only a combination of change in amplitude and phase without information about the direction can be observed. Because of the simplicity of this setup - no component has to be moved - and because of the possibility to convert this setup to the NIR-region, this method could be a candidate for in-process measurements.

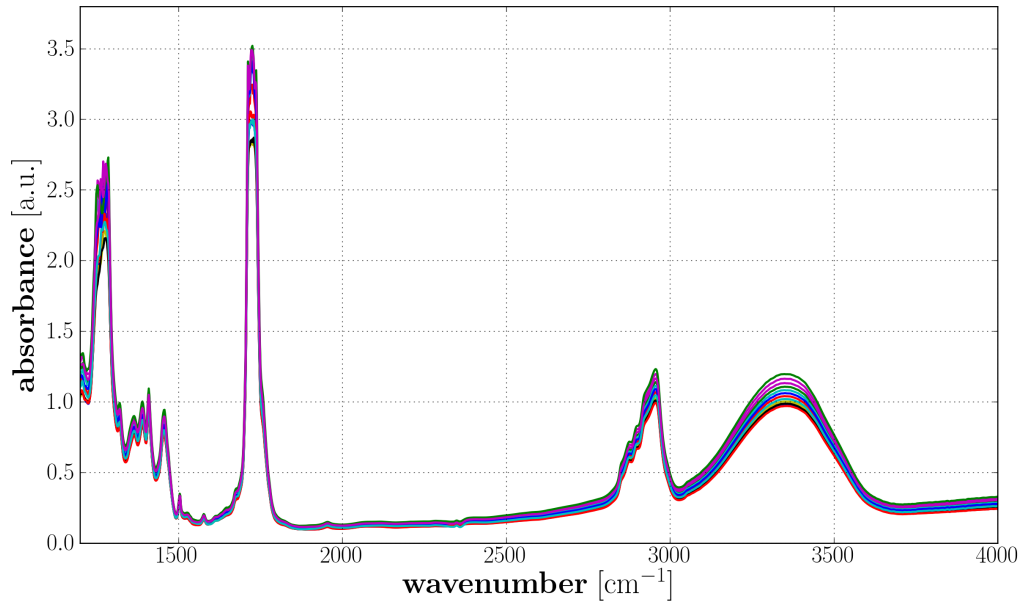


FIGURE 4.27: Classical absorbance spectra of the PLA film.

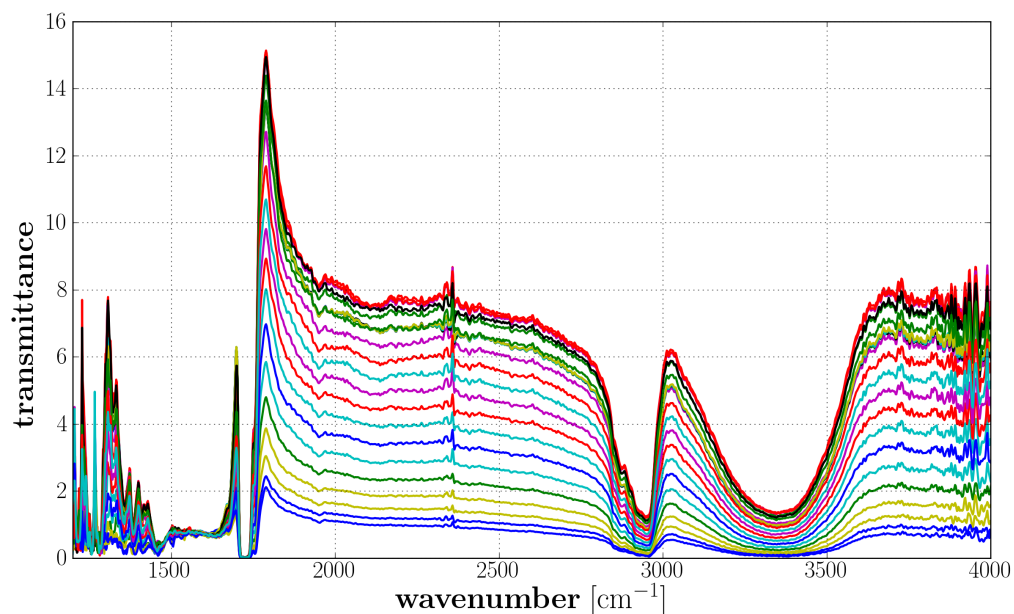


FIGURE 4.28: Transmittance spectra of the film at different stretching steps in crossed-polarizers configuration.

4.5 Error Estimation

The theoretical SNR described by equation 2.10 is difficult to determine experimentally, because first of all between the source and the detector there are many elements, namely mirrors, the beamsplitter and windows, but also the atmosphere inside the spectrometer, which all are wavenumber dependent and affect the spectrum. Secondly quantities as the throughput and the efficiency require either the consideration of misalignments of optical components inside the spectrometer or simplifying assumptions. Thirdly the influence of the detector and its possible geometrical and directional dependence is difficult to estimate and its detectivity is also wavenumber dependent. And ultimately, but also crucially, some of these influences can more or less change between measurements, thus devaluating a theoretical SNR. In reference [6] this SNR is evaluated with values which resemble the parameters used in the measurements of this work yielding the remarkably high value of $7,7 \times 10^4$.

A more practical approach to evaluate the performance of FTIR spectrometers is the measurement of 100% lines, which are simply measured by ratioing two spectra acquired under identical conditions of resolution and measurement time. A ratio of these two spectra indicates how the noise level varies across the spectrum. For mid-infrared FT-IR spectrometry it has become conventional to measure the noise level between 2000 and 2200 cm^{-1} , as the amplitude of the spectrum is usually maximal in this region and there is minimal interference by the absorption of atmospheric water vapor and CO_2 [6]. In figure 4.29 fifteen successive 100% lines are shown. The spectra are recorded in rapid-scan mode with the same detector and the same measurement parameters as the static IRLD measurements in section 4.2.1 and the measurements in the crossed-polarizer section 4.4.

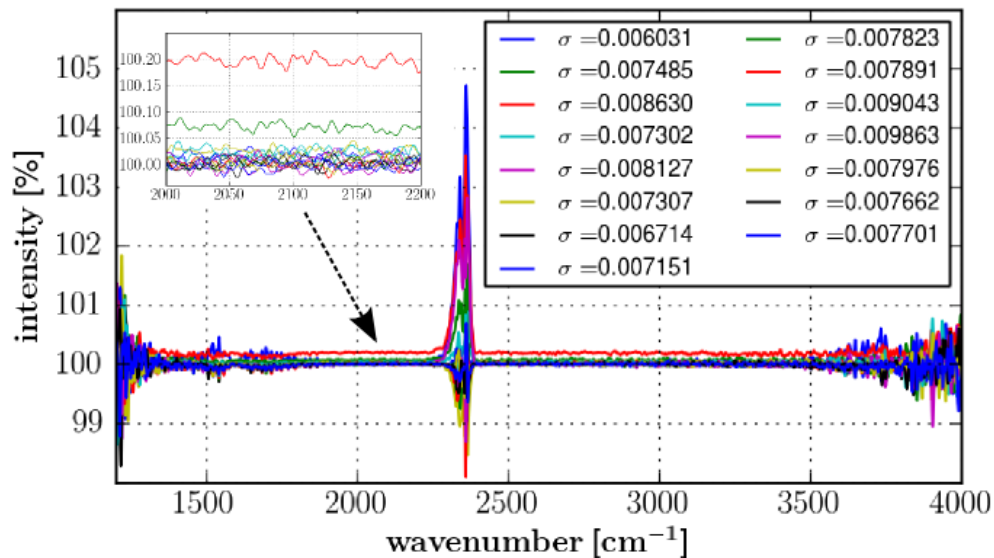


FIGURE 4.29: Fifteen successive 100% lines. In the upper left corner the lines are magnified in the region between 2000 and 2200 cm^{-1} . For each line the standard deviation σ was calculated for this specific region.

The big CO₂-peak at approximately 2350 cm⁻¹ and the two noisy features of the water vapor around 1500 cm⁻¹ and 3700 cm⁻¹ witness problematic atmospheric circumstances between the source and the detector. The atmosphere inside the spectrometer is insulated, and exchangeable dry-cartridges suppress high humidity, but cannot fully prohibit changes in the refractive index of the atmosphere over time. Outside the spectrometer the atmosphere certainly sustains big fluctuations, as the laboratory is a big room, where several people work and several computers and other electronic equipment heat up the room irregularly. Therefore the so-called '5 o'clock effect' has already become noticeable, that is, the performance is improving in the evening when many external perturbations are shut down. One remaining noise source, which plays a decisive role in step-scan mode and will be discussed further down, is erroneous sampling. In rapid-scan mode this would imply that the velocity of the moving mirror is not precisely constant throughout the scan, even though the interferogram is sampled at exactly equal intervals of retardation.

In regions where atmospheric perturbations have little influence the residual noise is produced by the detector. Thus the values of the standard deviation in figure 4.29 are good estimations of the detector noise. The highest value is 0,009863%, which is approximately five times the percental value of the digitization noise when the full range of the ADC is used. A general definition of the SNR is the reciprocal of the coefficient of variation, i.e. the ratio of mean μ to standard deviation σ of a signal. Ratioing the 100% of the signal and the mean of the standard deviations brings the SNR of 14285 which is approximately a fifth of the theoretical value. In figure 4.30 the mean of the sixteen recorded spectra from the 100% lines above is ratioed by the standard deviation at each spectral point leading to a more realistic SNR. And again the problematic atmospheric circumstances can be clearly seen, but also in the regions in between, the SNR is very low compared to the values above.

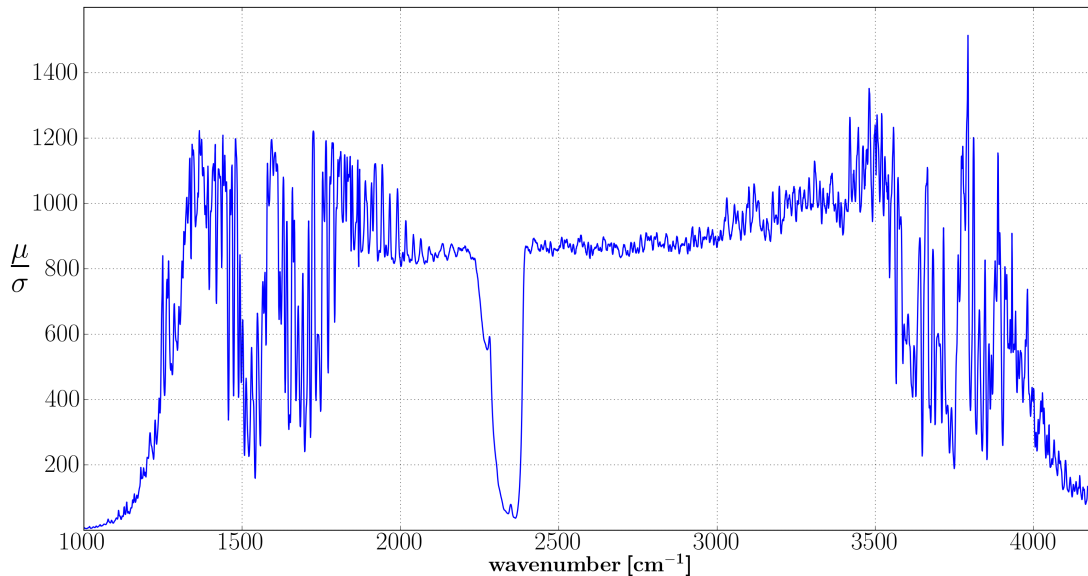


FIGURE 4.30: The calculated SNR from the ratio of the mean of 16 spectra and the standard deviation of each spectral point.

In rapid-scan mode FTIR spectroscopy is clearly a detector noise limited system depending on the thermal background of the detector. In contrast, many of the crucial noise sources affecting step-scan measurements are multiplicative¹¹ causing a significant SNR disadvantage of the step-scan mode provided that the same data collection time relative to conventional rapid-scan FTIR spectroscopy is used [32]. In table 4.4 probable noise sources are listed. Almost invariably, they are caused by fluctuations in temperature and are interdependent.

-
- Refractive index of air - mirror position error
 - Temperature of beamsplitter
 - Detector stability
 - Source temperature
 - Laser-amplitude and frequency stability
 - Mechanical stability with temperature
 - Mechanical vibrations of optics
-

TABLE 4.4: Potential sources of instability in step-scan FT-IR spectrometers, taken from reference [32]

Some possible noise sources such as source fluctuation, detector instability, laser amplitude and frequency instability and digitization noise can be neglected here. The optical bench of the FTIR spectrometer is made of aluminum, which has a large coefficient of thermal expansion, thus it is possible that the optical alignment can vary with temperature. The three main noise sources in the step-scan measurements in this thesis derive from mechanical vibrations of optics, path difference errors and fluctuation of the temperature of the beamsplitter, which are inherently multiplicative errors.

The optical efficiency of a beamsplitter can vary significantly with temperature. Especially the Germanium-layer has a large thermo-optical coefficient, which arises at least partly because of the small bandgap energy. This characteristic allows the population of charge carriers to vary rapidly with temperature. The variation is largest in the middle of the spectral range (at $\sim 2500 \text{ cm}^{-1}$) [32]. The convection inside the FTIR spectrometer is driven by dissipative heat from the reference laser, from the infrared source and from power supplies and electronic components. Any variation of temperature between the two arms of the interferometer results in a change of refractive index and therefore in a path difference error.

Mirror-position errors can arise from residual mirror oscillations after each mirror step or from mechanical vibrations depending on the experimental conditions. The optical bench is in no way mechanically damped, thus each vibration source in the environment can affect the position of the mirror. Mirror fluctuations can be monitored by measuring the signal generated by the HeNe laser beam passing through the interferometer, which is used to control the movement of the mirror. In figure 4.31 the laser signal is shown under three different conditions. In (a) the signal is recorded under rather stable conditions. The individual steps and

¹¹i.e., noise from these sources is proportional to the magnitude of the signal itself. The wideband noise from infrared detectors is additive, i.e., the magnitude of the noise is independent of the magnitude of the signal.

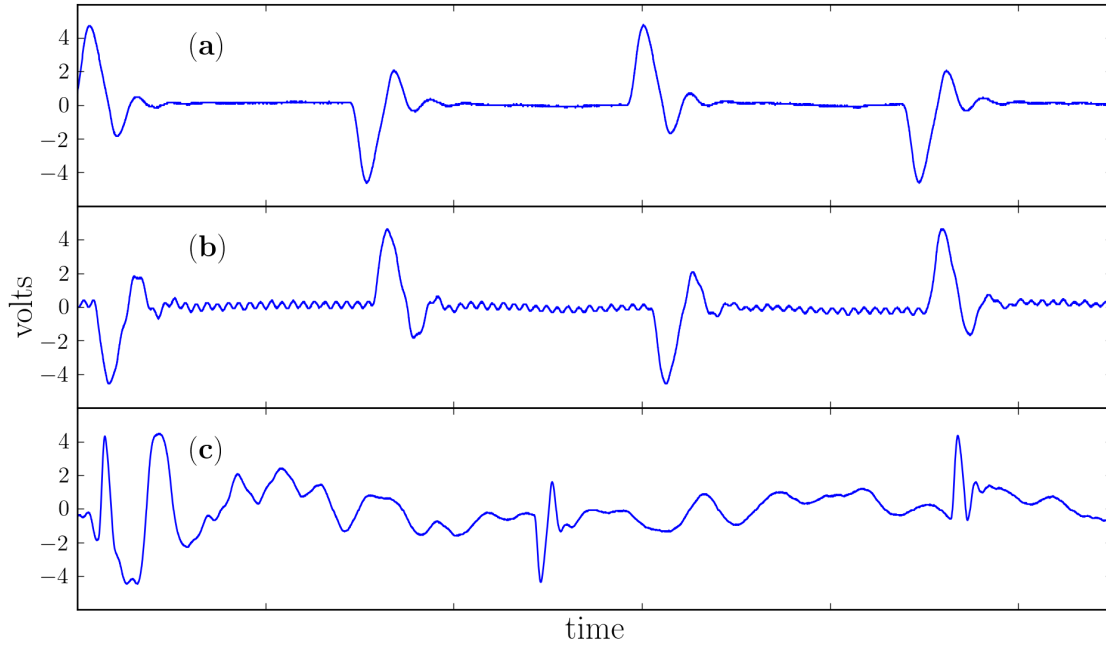


FIGURE 4.31: A small section of the signal generated by the HeNe laser in step-scan mode. The signal is measured in volts which are proportional to the position of the mirror.

the residual oscillations can be clearly seen, illustrating the need of a stabilization time before a measurement can be carried out. In (b) the signal is recorded while the experimenter is making a constant acoustical noise, which causes a sinusoidal vibration in the signal. In (c) the signal is recorded while the experimenter is stamping the floor causing large mirror displacements. These influences are largest near the zero path difference position, as in this region the signal variation is maximal. Mirror fluctuations introduce errors in the spacing of the interferogram sampling points, leading to an increase in spectral noise, but the distortions exhibit a rather weak wavenumber dependence. The distortions become relevant if the mirror fluctuations are larger than about $\pm 1,5$ nm [33]. The spectrometer software offers a test procedure in order to check the position accuracy of the mirror, determining the pendulum radius of the mirror by means of the laser signal. This procedure delivers the root mean square (rms) value of several deviation values in nanometers. It was carried out twenty times, some hours after 5 o'clock when there are few external perturbations. The rms values are always larger than 1,5 nm and yield a mean value of $5,21 \pm 11,32$ nm. These values indicate also that the experimental conditions are problematic for step-scan measurements, as the slightest vibration has an influence on the detected signal.

The key difference between rapid-scan and step-scan mode is the average mirror velocity, which alters the dynamic range of the detector signal as well as the frequencies of its components. The SNR disadvantage of step-scan mode is related to low-frequency multiplicative fluctuations, caused in part by temperature variations, which convolve noise with measured spectra. Refractive index variations of air in the paths of the infrared and laser radiation can be a particularly serious

temperature-induced problem [32]. Any multiplicative noise source of a frequency less than the separation between adjacent spectral elements will be efficiently rejected. There are a number of unstable optical and electronic elements in most FTIR spectrometers that fluctuate at frequencies much higher. The effect is that each point in a step-scan interferogram is multiplied by a random number near unity. Multiplication in the interferogram domain is equivalent to convolution in the spectral domain. Thus the spectrum is convolved with random multiplicative noise [32]. Because of the much shorter time scale of a single rapid-scan, fluctuations do not affect each point of the interferogram differently as in step-scan operation but rather affect all of the interferogram data points nearly equally. Therefore the multiplex advantage of FTIR spectroscopy degrades in the presence of multiplicative noise sources.

In figure 4.32 the 100% lines of the dc- and ac-component of an arbitrary polarization-modulated measurement are shown. The standard deviations in the region between 2000 and 2200 cm^{-1} are calculated and yield the $\text{SNR}_{dc}=322$ and the $\text{SNR}_{ac}=199$. The SNR of rapid-scan mode is therefore approximately 50 times higher than in step-scan mode. The spectral features caused by water vapor and CO_2 are again present in the 100% lines, but the useful area of the spectra is fairly narrowed, because the modulation of a noisy signal rather increases the already existing noise.

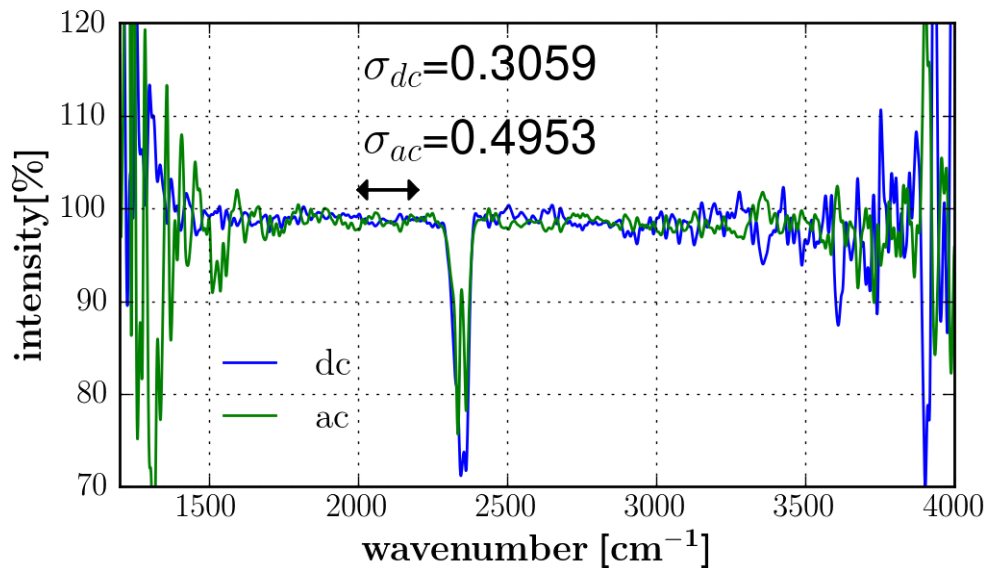


FIGURE 4.32: The 100% lines of the dc- and ac-component of a polarization modulated measurement.

5. Conclusions

Exploiting the change of polarization of infrared light passing through the sample in FTIR spectroscopy offers the application of various measurement methods, which give spectral information about the orientation of molecules. This additional information is important, as the microscopic structures are directly related to the macroscopic properties. Three different measurement methods were carried out, IRLD (static and polarization-modulated), PMSE and FTIR spectroscopy in crossed-polarizers configuration, in order to achieve information about the orientation of the molecules of a PLA film during uniaxial elongation.

The infrared linear dichroism experiment is well suited in order to study the behavior of multicomponent systems such as polymers, since the orientation of the different components can be distinguished. It was possible to resolve the change in orientation of the different functional groups of the PLA film through the stretching process. IRLD also supplies information on hydrogen-bonding interactions and molecular-level insight into the tensile properties. So it was possible to reveal the prestretching of the PLA film induced by the manufacturing process, which forces the backbone of the macromolecules to align and gives preferable tensile properties.

The experiments between crossed polarizers are sensitive to any change in polarization and promise great potential for process implementation. If the change without distinction between amplitude and phase can give sufficient information, this setup will be clearly favoured because of its simplicity.

The most powerful technique is spectroscopic ellipsometry, as it is possible to receive the complex refractive index, respectively the change in amplitude and phase separately. The full benefit of this method as well as of the application of polarization modulation can not be shown in this thesis. The experimental conditions are not yet suitable for accurate step-scan operation.

The error estimation section clearly shows that external vibrational perturbations along with temperature fluctuations can be a source of excessive noise in step-scan FTIR spectroscopy. In order to decrease the sensitivity to instrument vibrations from building motion or acoustic noise and to low-frequency multiplicative fluctuations, a pneumatically damped optical bench will be installed. One important conclusion, which can be drawn from all measurements, is that there is a diversity of external but also of internal influences affecting the spectra from FTIR spectroscopy, especially in step-scan operation, and even more when using polarized light.

Besides the further development and improvement of the existing measurement setups, polarized FTIR spectroscopy opens the way to investigations of surface layers. By means of reflection measurements the two polarization components

show a different behavior in phase and amplitude depending on the angle of incidence and on the substrate and layers. The two methods which will be applied are infrared reflection absorption spectroscopy (IRRAS) and reflection anisotropy spectroscopy (RAS). In summary FTIR spectroscopy enables many extensions making the technique suitable for virtually any sample, delivering information over a broad spectral region, restricting the experimenter in no way and offering a really wide area of application.

Appendix A

Jones Calculus

When the light is fully polarized, the Jones calculus is sufficient for the description of the state of polarization. Each state can be represented as the vector sum of the components of the electric field vector in two mutually orthogonal directions perpendicular to the direction of propagation. Considering a monochromatic plane wave with angular frequency ω and angular wavenumber k , propagating along z -direction, the polarization state of light is fully described as the vector sum of the electric fields \mathbf{E}_x and \mathbf{E}_y , which are elements of the vector space over the complex numbers:

$$\begin{aligned}\mathbf{E}(z, t) &= \mathbf{E}_x(z, t) + \mathbf{E}_y(z, t) \\ &= \{E_{x0} \exp[\imath(\omega t - kz + \delta_x)]\} \hat{\mathbf{x}} + \{E_{y0} \exp[\imath(\omega t - kz + \delta_y)]\} \hat{\mathbf{y}}\end{aligned}\quad (\text{A.1})$$

where $\hat{\mathbf{x}}$ and $\hat{\mathbf{y}}$ are unit vectors and δ_x and δ_y the initial phases. The electric field vector then is:

$$\mathbf{E}(z, t) = \begin{bmatrix} E_{x0} \exp\{\imath(\omega t - kz + \delta_x)\} \\ E_{y0} \exp\{\imath(\omega t - kz + \delta_y)\} \end{bmatrix} = \exp\{\imath(\omega t - kz)\} \begin{bmatrix} E_{x0} \exp(\imath\delta_x) \\ E_{y0} \exp(\imath\delta_y) \end{bmatrix} \quad (\text{A.2})$$

The Jones vector then is defined by:

$$\hat{\mathbf{J}} := \begin{bmatrix} E_{x0} \exp(\imath\delta_x) \\ E_{y0} \exp(\imath\delta_y) \end{bmatrix} \quad (\text{A.3})$$

and introducing the phase difference $\Delta = (\delta_x - \delta_y)$ yields:

$$\hat{\mathbf{J}} = \begin{bmatrix} E_{x0} \exp(\imath\Delta) \\ E_{y0} \end{bmatrix} \exp(\imath\delta_y) \quad (\text{A.4})$$

The light intensity I is then given by:

$$I = I_x + I_y = |E_x|^2 + |E_y|^2 = E_{x0} E_{x0}^* + E_{y0} E_{y0}^* \quad (\text{A.5})$$

which cancels out the phase. However only the relative changes in amplitude and phase are of interest, that is why a normalized light intensity $I = 1$ is commonly used in the Jones calculus. In table A.1 some Jones vectors of different states of polarization are listed.

Polarization	Jones vector
Linear polarization parallel to x axis	$\begin{bmatrix} 1 \\ 0 \end{bmatrix}$
Linear polarization parallel to y axis	$\begin{bmatrix} 0 \\ 1 \end{bmatrix}$
Linear polarization oriented at 45°	$\frac{1}{\sqrt{2}} \begin{bmatrix} 1 \\ 1 \end{bmatrix}$
Right-circular polarization	$\frac{1}{\sqrt{2}} \begin{bmatrix} 1 \\ i \end{bmatrix}$
Left-circular polarization	$\frac{1}{\sqrt{2}} \begin{bmatrix} 1 \\ -i \end{bmatrix}$

TABLE A.1: Representations of states of polarization by the Jones vectors

Optical elements are represented by their Jones matrices. The Jones matrix of a polarizer \mathbf{P} with transmission axis parallel to the x-axis and in principle axis system (x,y) is expressed by

$$\mathbf{P}(0) = \begin{bmatrix} 1 & 0 \\ 0 & 0 \end{bmatrix} \quad (\text{A.6})$$

Rotations of optical elements can be performed by means of a coordinate rotation with the rotation matrices (counterclockwise and clockwise):

$$\mathbf{R}(\alpha) = \begin{bmatrix} \cos \alpha & \sin \alpha \\ -\sin \alpha & \cos \alpha \end{bmatrix} \quad \mathbf{R}(-\alpha) = \begin{bmatrix} \cos \alpha & -\sin \alpha \\ \sin \alpha & \cos \alpha \end{bmatrix} \quad (\text{A.7})$$

Thus for a polarizer as in equation A.6 the Jones Matrix transforms to:

$$\mathbf{P}(\alpha) = \mathbf{R}(-\alpha) \mathbf{P}(0) \mathbf{R}(\alpha) \quad (\text{A.8})$$

Appendix B

Mertz Method

As mentioned in section 2.2.3 the interferogram produced by the FTIR spectrometer generally comprises components which have an erroneous phase causing a spectrum with an imaginary part. However, the imaginary part doesn't represent anything physically reasonable, therefore the Mertz method [34] has to take care of the phase correction. In equation 2.6 the spectrum is achieved by means of a cosine Fourier transformation neglecting the asymmetry of the interferogram. A complex Fourier transformation takes care of this fact and is given by:

$$S'(\nu) = \int_{-\infty}^{+\infty} I(\delta) \exp(-i2\pi\nu\delta) d\delta \quad (\text{B.1})$$

The spectrum is then calculated by the complex addition:

$$S'(\nu) = \text{Re}(S'(\nu)) + i \text{Im}(S'(\nu)) \quad (\text{B.2})$$

where $\text{Re}(S'(\nu))$ is the real part and $\text{Im}(S'(\nu))$ is the imaginary part of the spectrum which is dispersed into two complex planes by the phase. The magnitude spectrum of $S'(\nu)$ is given by:

$$|S'(\nu)| = \sqrt{\text{Re}(S'(\nu))^2 + \text{Im}(S'(\nu))^2} \quad (\text{B.3})$$

which exhibits no phase error. These two spectra are related via:

$$S'(\nu) = |S'(\nu)| \exp(i\theta) \quad (\text{B.4})$$

The real spectrum is therefore given by:

$$\begin{aligned} S(\nu) &= S'(\nu) \exp(-i\theta) \\ &= \text{Re}(S'(\nu)) \cos \theta + \text{Im}(S'(\nu)) \sin \theta \end{aligned} \quad (\text{B.5})$$

The clue of the Mertz method is to calculate the phase angle from a short, symmetrically sampled interferogram and subsequently apply it to a much higher resolution spectrum. The algorithm used in this thesis resembles the algorithm from

the book [6], which is also presented by Delmar Larsen on the [ChemWiki](http://chemwiki.ucdavis.edu/Analytical_Chemistry/Instrumental_Analysis/Spectrometer/How_an_FTIR_instrument_works)-website¹ of the University of California, Davis. Here the explicit algorithm is not carried out, but the single steps are illustrated.

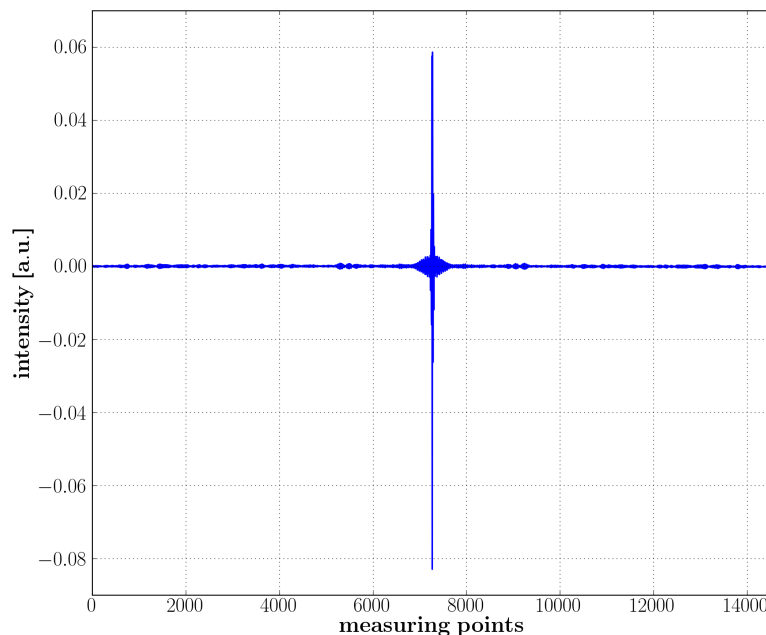


FIGURE B.1: A raw interferogram recorded by the ADC of the spectrometer.

In figure B.1 an interferogram recorded by the 24-bit ADC of the spectrometer is shown. A simple Fourier transformation of this interferogram would deliver an uncorrected spectrum. The first step of the Mertz algorithm is to cut out a small symmetric region (512 measuring points) around the centerburst, see figure B.2.

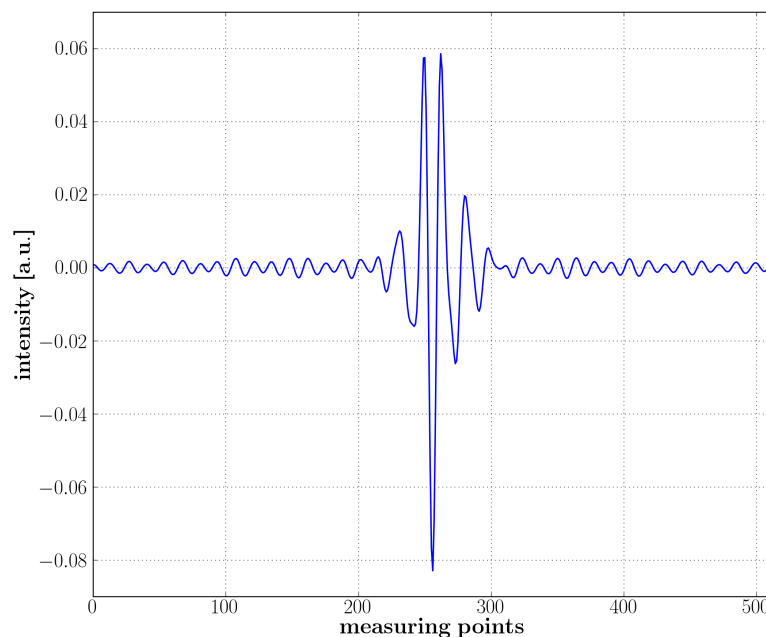


FIGURE B.2: 512 measuring points around the centerburst.

¹http://chemwiki.ucdavis.edu/Analytical_Chemistry/Instrumental_Analysis/Spectrometer/How_an_FTIR_instrument_works (last visited January 24, 2012)

In this region the interferogram has a large amplitude, as the components of various frequencies add constructively in phase. This location may be called a place of stationary phase.

The apodization of the spectra used in this thesis was accomplished by means of the Blackman–Harris apodization function which performs a considerable reduction of the amplitudes of the sidelobes, see figure B.3. The measuring points of the x-axis actually coincide with the path difference between the two optical paths inside the interferometer. The interferogram theoretically consists purely of cosines which have their maximum at the zero-point, thus the centerburst actually belongs to the border, which is executed in figure B.4.

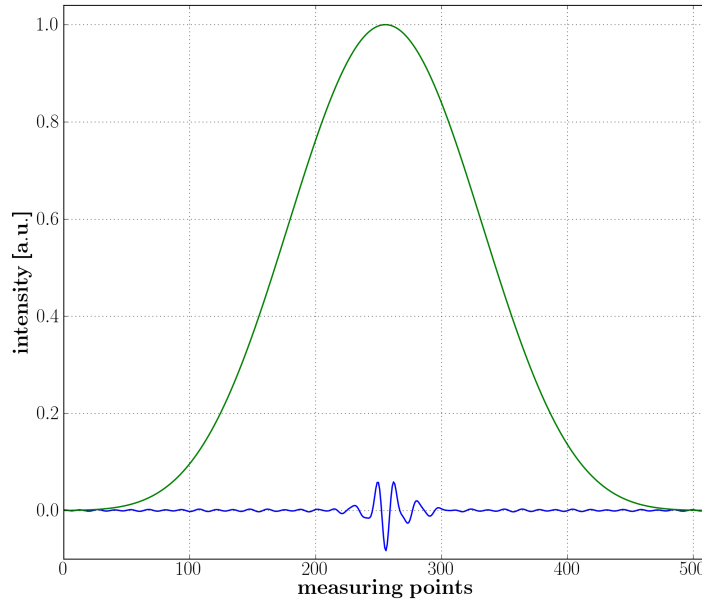


FIGURE B.3: The Blackman–Harris apodization function and the apodized interferogram.

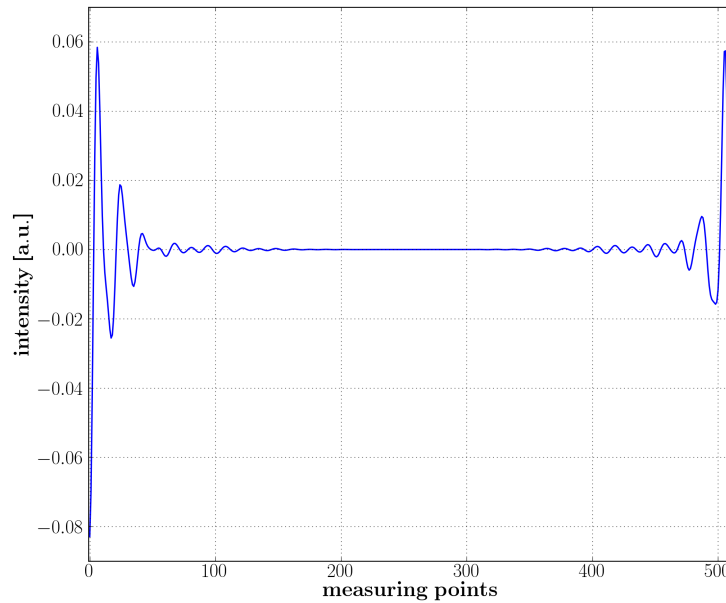


FIGURE B.4: The apodized interferogram is simply rotated such that the centerburst lies at 0.

In figure B.5 the spectrum delivered by Fourier transformation is shown, which consists of a real and a imaginary part. The real part is negative, because the single peak of the interferogram points in the negative direction. Therefore at the end of the algorithm the modulus is taken. The phase curve is shown in figure B.6, which is computed by taking the arc tangent of the ratio of the imaginary and the real part of the spectrum. The sine and the cosine of the phase is shown in figure B.7, which have to be interpolated to the size of the complete interferogram.

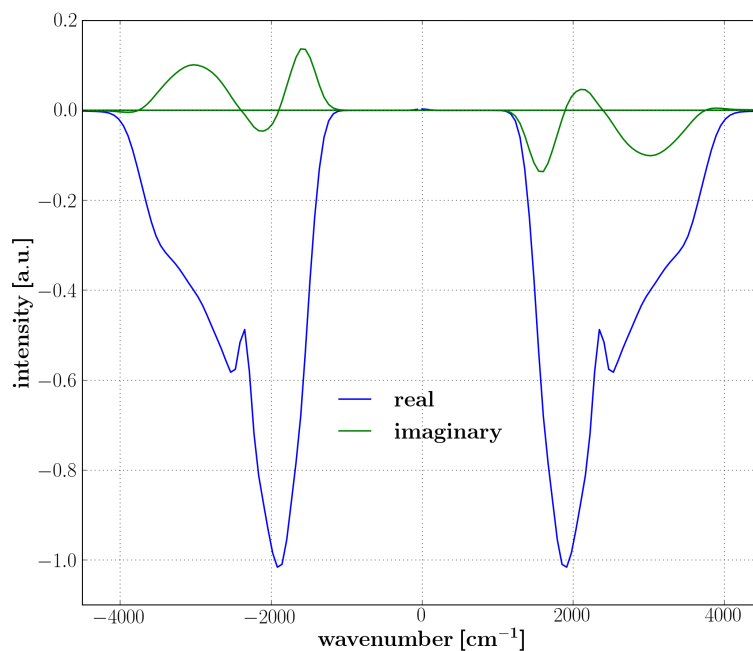


FIGURE B.5: The real and the imaginary part of the spectrum delivered by Fourier transformation.

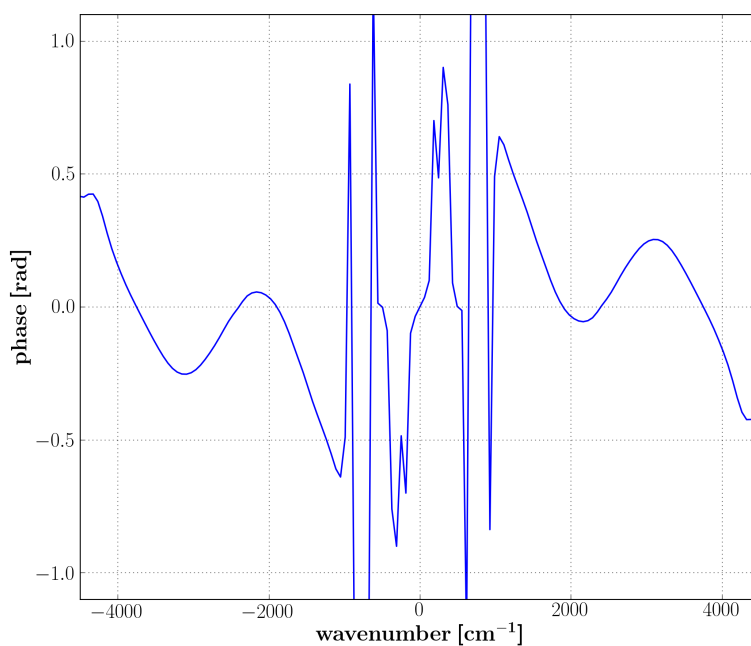


FIGURE B.6: The phase curve of the complex spectrum.

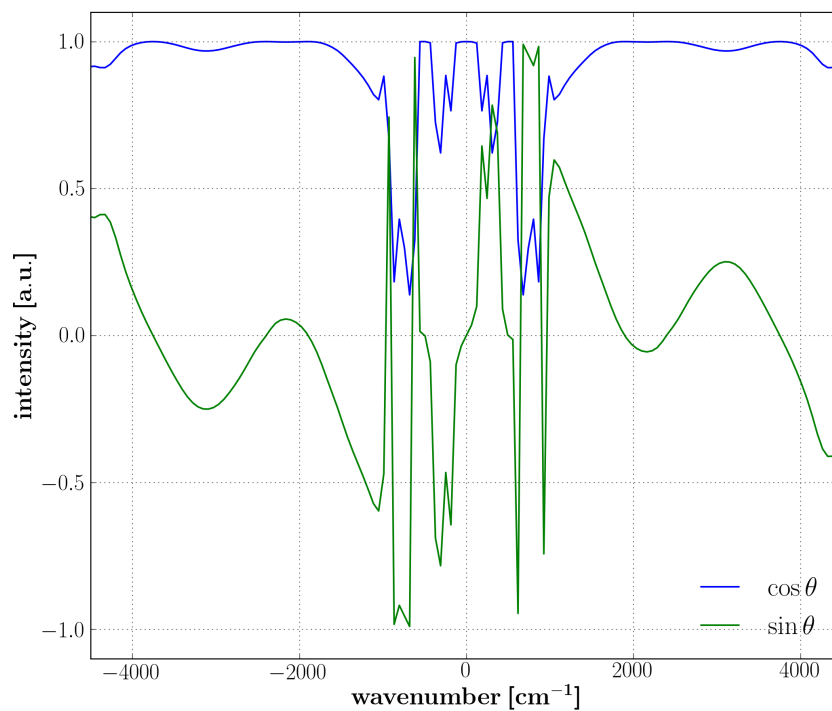


FIGURE B.7: The sinus and the cosine of the phase.

In this way the correction terms from equation B.5 are derived. Following the same procedure for the complete interferogram yields the complex spectrum in figure B.8.

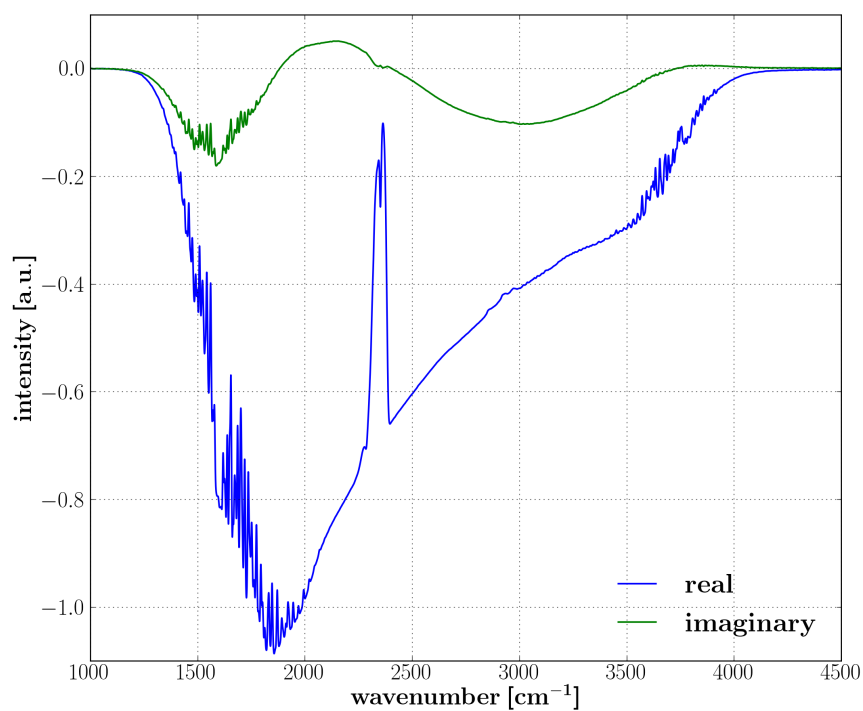


FIGURE B.8: The real and the imaginary part of the spectrum from the complete interferogram.

According to equation B.5 the real part of the spectrum is multiplied by the cosine and the imaginary part by the sine of the phase from figure B.7. This brings the corrected parts of the spectrum in figure B.9, whereas the sum of these two parts builds the real corrected spectrum shown in figure B.10. In this figure the spectrum calculated without any phase correction is also shown.

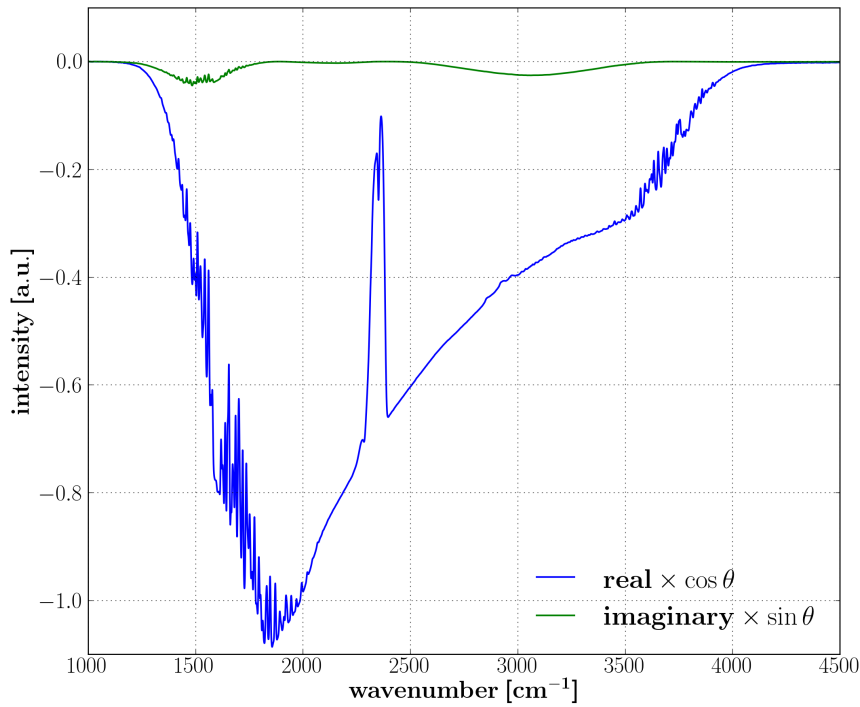


FIGURE B.9: The corrected real and imaginary part of the spectrum.

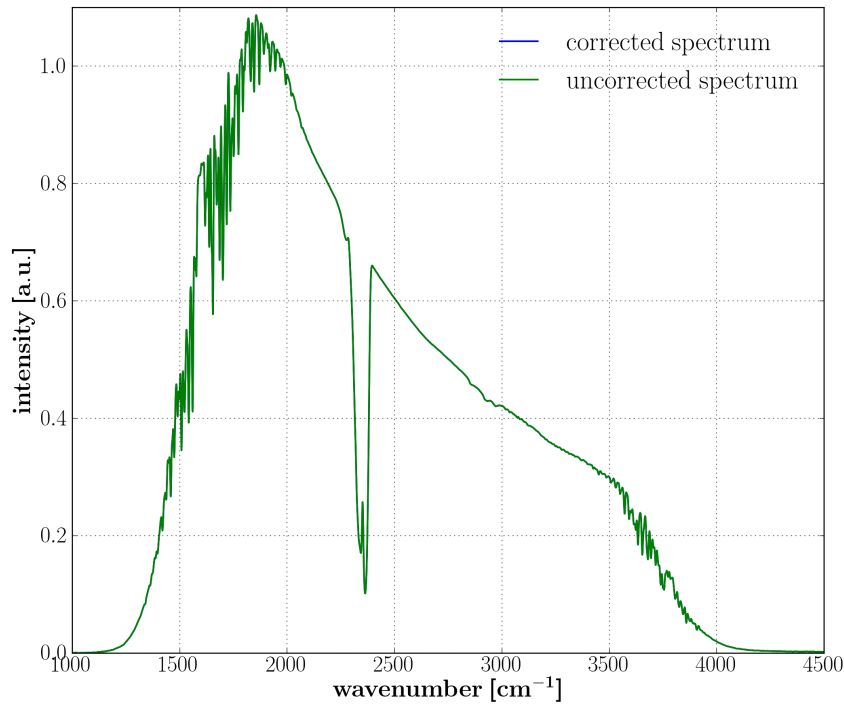


FIGURE B.10: The Mertz-corrected spectrum together with the uncorrected spectrum.

The subtraction of the uncorrected spectrum from the corrected spectrum, shown in figure B.11, reveals solely a very small difference between these spectra, which is rapidly increasing at the left border.

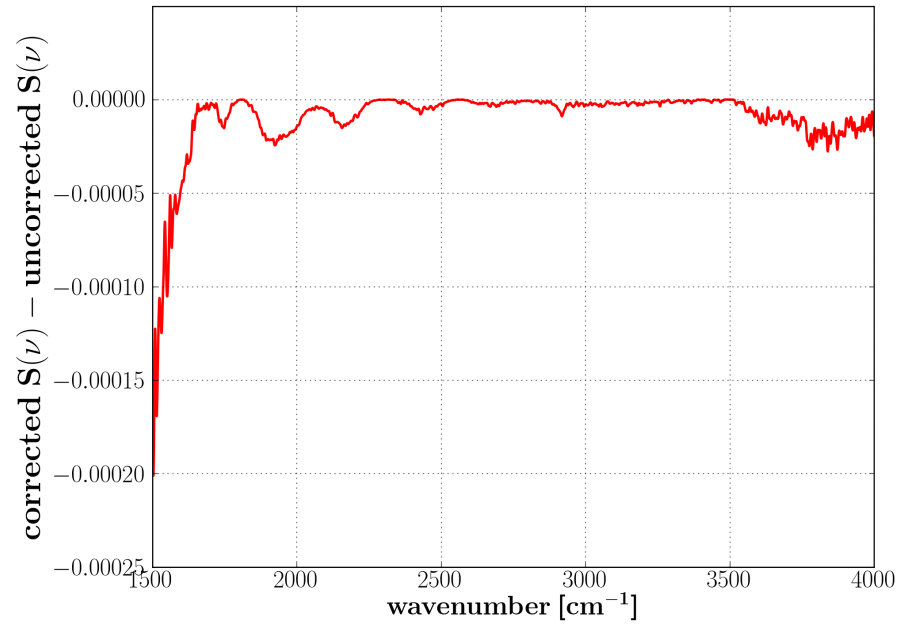


FIGURE B.11: The difference of the corrected and the uncorrected spectrum.

Bibliography

- [1] D.W. Krevelen and K. Te Nijenhuis. *Properties of Polymers: Their Correlation With Chemical Structure; Their Numerical Estimation and Prediction from Additive Group Contributions*. Elsevier, 2009.
- [2] J. Ren. *Biodegradable Poly (Lactic Acid): Synthesis, Modification, Processing and Applications*. Springer, 2011.
- [3] Jasim Ahmed and Sunil K. Varshney. Polylactides—Chemistry, Properties and Green Packaging Technology: A Review. *International Journal of Food Properties*, 14(1):37–58, 2011.
- [4] Shuhui Kang, Shaw Ling Hsu, Howard D. Stidham, Patrick B. Smith, M. Anne Leugers, and Xiaozhen Yang. A Spectroscopic Analysis of Poly(lactic acid) Structure. *Macromolecules*, 34(13):4542–4548, 2001.
- [5] Vukovic-Kwiatkowska and H. Kaczmarek I. Preparation and characterization of interpenetrating networks based on polyacrylates and poly(lactic acid) . *eXPRESS Polymer Letters*, 6(1):78–94, 2012.
- [6] P. Griffiths and J.A. De Haseth. *Fourier Transform Infrared Spectrometry*. Chemical Analysis: A Series of Monographs on Analytical Chemistry and Its Applications. Wiley, 2007.
- [7] S.R. Sandler. *Polymer Synthesis and Characterization: A Laboratory Manual*. Academic Press, 1998.
- [8] Jyrki Kauppinen and Jari Partanen. *Fourier Transforms in Spectroscopy*. Wiley-Vch, 2001.
- [9] Max Born and Emil Wolf. *Principles of Optics: Electromagnetic Theory of Propagation, Interference and Diffraction of Light (7th Edition)*. Cambridge University Press, 7th edition, 1999.
- [10] Asma Al-Qasimi, Olga Korotkova, Daniel James, and Emil Wolf. Definitions of the degree of polarization of a light beam. *Opt. Lett.*, 32(9):1015–1016, May 2007.
- [11] F. Agulló-López, J.M. Cabrera, and F. Agulló-Rueda. *Electrooptics: Phenomena, Materials and Applications*. Lasers and optical engineering. Academic Press, 1994.

- [12] G.A. Reider. *Photonik: Eine Einführung in die Grundlagen*. Springer-Lehrbuch : Technik. Springer, 2004.
- [13] T. Buffeteau and M. Pézolet. Linear Dichroism in Infrared Spectroscopy. *Handbook of Vibrational Spectroscopy*, 2001.
- [14] H. Fujiwara. *Spectroscopic Ellipsometry: Principles and Applications*. Wiley, 2007.
- [15] Hinds Instruments, Inc. PEMs in ellipsometry. *application note*, 2009 (last visited January 24, 2012). URL http://www.hindsinstruments.com/wp-content/uploads/Calculating_Psi_and_Delta1.pdf. (last visited January 24, 2012).
- [16] KW Hipps and GA Crosby. Applications of the photoelastic modulator to polarization spectroscopy. *Journal of Physical Chemistry*, 83(5):555–562, 1979.
- [17] H.G. Tompkins and E.A. Irene. *Handbook of Ellipsometry*. William Andrew Pub., 2005.
- [18] A. Canillas, E. Pascual, and B. Dré villon. Phase-modulated ellipsometer using a Fourier transform infrared spectrometer for real time applications. *Review of scientific instruments*, 64(8):2153–2159, 1993.
- [19] M. J. Dignam, B. Rao, M. Moskovits, and R. W. Stobie. Ellipsometric Determination of the Spectra of Adsorbed Molecules. *Canadian Journal of Chemistry*, 49(7):1115–1132, 1971.
- [20] T. Buffeteau, B. Desbat, and J. M. Turel. Polarization Modulation FT-IR Spectroscopy of Surfaces and Ultra-thin Films: Experimental Procedure and Quantitative Analysis. *Appl. Spectrosc.*, 45(3):380–389, Mar 1991.
- [21] Vlad Zamlynnny. *Electrochemical and Spectroscopic Studies of Pyridine Surfactants at the Gold-Electrolyte Interface*. PhD dissertation, The University of Guelph, Canada, 2002.
- [22] C. E. Shannon. Communication in the presence of noise. In *Proceedings of the Institute of Radio Engineers (IRE)*, volume 37, pages 10–21, 1949.
- [23] BRUKER OPTIK GmbH. VERTEX 70 Benutzerhandbuch. 2004. URL <http://www.brukeroptics.com>. (last visited January 24, 2012).
- [24] Hinds Instruments, Inc. PEM-90 Photoelastic Modulator Systems, User Manual. 1998. URL <http://www.hindsinstruments.com>. (last visited January 24, 2012).
- [25] Boston Electronics Corporation. IR Detectors from Vigo System, Datasheet. URL <http://www.vigo.com.pl>. (last visited January 24, 2012).
- [26] ADLINK TECHNOLOGY INC. PXI-9816 User’s Manual. 2008. URL <http://www.adlinktech.com>. (last visited January 24, 2012).

- [27] W.M. Lai, D.H. Rubin, D. Rubin, and E. Krempel. *Introduction to Continuum Mechanics*. Elsevier Science, 2009.
- [28] Haochuan Wang, Darla K. Graff, Jon R. Schoonover, and Richard A. Palmer. Static and Dynamic Infrared Linear Dichroic Study of a Polyester/Polyurethane Copolymer Using Step-Scan FT-IR and a Photoelastic Modulator. *Appl. Spectrosc.*, 53(6):687–696, Jun 1999.
- [29] Darla K. Graff, Haochuan Wang, Richard A. Palmer, and Jon R. Schoonover. Static and Dynamic FT-IR Linear Dichroism Studies of Plasticization Effects in a Polyurethane Elastomer. *Macromolecules*, 32(21):7147–7155, 1999.
- [30] Jon R. Schoonover, Darla Graff Thompson, Jill C. Osborn, E.Bruce Orler, Debra A. Wroblewski, Anderson L. Marsh, Haochuan Wang, and Richard A. Palmer. Infrared linear dichroism study of a hydrolytically degraded poly(ester urethane). *Polymer Degradation and Stability*, 74(1):87–96, 2001.
- [31] Shunji Nomura, Ryohei Ashitani, Hideya Matsuda, and Lameck Banda. Dynamic infrared spectroscopic studies on structure of segmented poly(urethaneurea). *Polymer*, 42(21):9045–9049, 2001.
- [32] Christopher J. Manning and Peter R. Griffiths. Noise Sources in Step-Scan FT-IR Spectrometry. *Appl. Spectrosc.*, 51(8):1092–1101, Aug 1997.
- [33] C. Rodig and F. Siebert. Errors and Artifacts in Time-Resolved Step-Scan FT-IR Spectroscopy. *Appl. Spectrosc.*, 53(8):893–901, Aug 1999.
- [34] L. Mertz. Auxiliary computation for Fourier spectrometry. *Infrared Physics*, 7(1):17–23, 1967.

Zusammenfassung

Fourier-Transform Infrarotspektroskopie (FTIR) ist ein etabliertes Messverfahren in der industriellen Prozessanalyse, bei der derzeit noch weitestgehend auf die Messung der Änderung der Polarisierung des Lichtes, hervorgerufen durch die Probe (durch Reflexion oder Transmission), verzichtet wird. Diese Änderung enthält jedoch je nach verwendetem Messaufbau wichtige zusätzliche Informationen über das zu untersuchende Material, und polarisationsabhängige Messungen führen im Allgemeinen zu einer höheren Sensitivität der Messung.

In dieser Arbeit werden drei verschiedene polarisationsabhängige Messmethoden in Transmission angewendet, und zwar statische sowie polarisationsmodulierte Linear-Dichroismus Messungen (PM-IRLD), polarisationsmodulierte spektroskopische Ellipsometrie (PMSE) und FTIR-Spektroskopie in einer Konfiguration zwischen gekreuzten Polarisatoren, um Informationen über die Ausrichtung der Moleküle einer Polymilchsäurefolie (PLA) während eines Zugversuchs zu erhalten. Die Anwendung der Polarisationsmodulation verspricht eine Erhöhung der Messgenauigkeit durch Kompensation der Umwelteinflüsse. Im Zuge dieser Arbeit wurde ein neuer, flexibler, computergesteuerter Messaufbau mit dazugehöriger digitaler Signalverarbeitung und mit Anbindung an das bereits bestehende FTIR-Spektrometer entwickelt. Dieser Aufbau ermöglicht die Anwendung der verschiedenen polarisationsabhängigen Messmethoden und hat deren Weiterentwicklung und Adaptierung für das industrielle Prozessumfeld zum Ziel.

Die Resultate zeigen, dass mit Hilfe dieser Messmethoden die Änderung der Orientierung der einzelnen Moleküle der PLA-Folie während des Zugversuchs gemessen werden kann. Die verschiedenen Methoden unterscheiden sich jedoch noch sehr in ihren Signal-Rausch-Verhältnissen und vor allem die Methoden mit Polarisationsmodulation erfordern diesbezüglich Verbesserungen. Die Ergebnisse sind aber vielversprechend für die weiteren prozessnahen Untersuchungen und die kommenden polarisationsabhängigen Reflexionsmessungen, die ebenfalls mit diesem Messaufbau durchgeführt werden können.

Jakob Kilgus

✉ jakob.kilgus@gmail.com

Personal data

Date of birth **May 29th, 1980.**
Place of birth **Vöcklabruck, Austria.**
Nationality **Austrian.**
Marital status **civil partnership with Nora Staudinger, two sons Juri and Mattis.**

Education

2006 – 2013 **Study of Physics, *University of Vienna.***
1998 – 2001 **Study of Chemistry and German Language and Literature, *University of Vienna,***
teaching profession, abandon of studies without degree.
1990 – 1998 **Secondary school, *Vöcklabruck.***
1986 – 1990 **Primary school, *Vöcklabruck.***

Work experience

Oct. 2011 – **Research scientist, *RECENDT, Linz.***
2007 – 2009 **Freelance worker, *Artex Art Services, Vienna.***
Frequently
Mar. – Sept. 2006 **Machine operator, *S.Spitz GmbH, Attnang-Puchheim.***
Aug. – Nov. 2005 **Carpenter, *HolzArt, Timelkam.***
Nov. 2003 – Sept. 2005 **Carpenter apprenticeship, *HolzArt, Timelkam.***
Oct. 2002 – Sept. 2003 **Laboratory assistant, *Lenzing AG.***
Oct. 2001 – Sept. 2002 **Alternative national service, *Lebenshilfe Oberösterreich.***

Languages

German **Mothertongue**
English **Fluent**
French **Basic**

Basic words and phrases only